Chemical Science

ROYAL SOCIETY OF CHEMISTRY

PERSPECTIVE

View Article Online
View Journal | View Issue

Check for updates

Cite this: *Chem. Sci.*, 2025, **16**, 9577

All publication charges for this article have been paid for by the Royal Society of Chemistry

Rethinking boron's role in intramolecular charge transfer: from an acceptor to a donor–acceptor regulator

Jiaqi Dong,† Lingjuan Chen† and Deng-Tao Yang *

Received 11th March 2025
Accepted 8th May 2025

DOI: 10.1039/d5sc01916h

rsc.li/chemical-science

In-depth exploration of charge transfer contributes directly to the comprehension of the microscopic mechanisms underlying life processes while accelerating progress in the cutting-edge fields of organic electronics. At the molecular level, the boron atom with its unique empty p-orbital has been widely exploited to construct intramolecular charge transfer (ICT) molecules. This perspective seeks to thoroughly examine the types and emerging mechanisms of ICT in both tricoordinate and tetracoordinate organoboron-based ICT molecules (OBCTs), thereby clarifying boron's role in the ICT process. With respect to three-coordinated OBCTs, organoboron molecules with distinct CT pathways and distances are discussed in terms of their development history, CT mechanisms and structure–property relationships, which can provide guidance for designing highly sought-after molecules. For four-coordinated OBCTs, emerging CT mechanisms and the role of coordination in modulating CT properties are discussed, indicating substantial opportunities for the development of CT in these systems. In addition, the development of novel CT mechanisms or the integration of multiple CT processes holds promise for overcoming existing limitations in current OBCTs. Coupling the advancement of CT mechanisms with the discovery of innovative application scenarios is poised to propel the future progression of OBCTs.

1. Introduction

"Life is nothing but an electron looking for a place to rest"—Albert Szent-Györgyi. Nearly all life forms on Earth rely, directly or indirectly, on charge transfer (CT) processes for survival, which are one of the critical steps in photosynthesis, biological signal transduction, and various forms of energy conversion.[1,2] At the molecular level, intramolecular charge transfer (ICT) involves electron transfer from an electron-rich segment to an electron-deficient segment within the same molecule.[3] ICT has been extensively studied as a foundational mechanism in molecular photophysics and photochemistry[3,4] and is integral to applications in organic dyes,[5] biotechnology,[6,7] organic optoelectronic devices,[8] nonlinear optics (NLO),[9] and sensing.[10,11] A common approach to enhance ICT is the incorporation of an electron-donating (D) unit and an electron-accepting (A) unit, typically linked by a conjugated linker. The ICT process inherently involves the separation of positive and negative charges, whereas the ideal condition of complete charge separation is referred to as the charge-separated (CS) state (D^+–A^-).[1,3] The CS state can be considered a pure charge-transfer state, comprising a radical cation ($D^{\bullet+}$) and a radical anion ($A^{\bullet-}$). In D–π–A molecules, the CS state can be represented by resonance structures (*i.e.*, the molecular dipolar forms), which offer an intuitive and convenient way to analyze the excited-state electron distribution with strong CT character (Fig. 1a). Selection of appropriate donor and acceptor units is crucial to define the expected ICT properties.

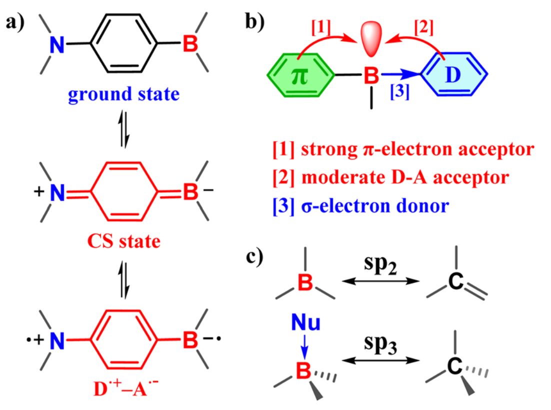

Fig. 1 (a) CS state of organoboron compounds upon excitation. (b) Role of tricoordinate boron as an electron acceptor. (c) Similar bonding characteristics of boron and carbon.

Xi'an Key Laboratory of Hybrid Luminescent Materials and Photonic Device, School of Chemistry and Chemical Engineering, Northwestern Polytechnical University, Xi'an, Shaanxi 710072, China. E-mail: dtyang@nwpu.edu.cn

† These authors contributed equally to this work.

Boron atoms with vacant p-orbitals rank among the most unique ICT acceptors.[12–18] Compared to other electron-deficient or highly electronegative acceptors such as pyridine, cyano and fluoride, boron provides distinctive features: (a) tricoordinate boron acts as a strong π-electron acceptor with its empty p-orbital prone to being filled by electron delocalization in an electron-rich D–A system, resulting in a moderate acceptor. Additionally, the low electronegativity of boron enables it to act as a σ-electron donor. These characteristics allow the boron atom to effectively separate frontier molecular orbitals (FMOs) and avoid a strong CT process that can lead to transition-forbidden states and low oscillator strength (Fig. 1b), (b) boron exhibits similar bonding characteristics to carbon (Fig. 1c), allowing it to integrate into organic skeletons.[19–22] The dual role of boron as both an acceptor and a structural component of the molecular backbone offers a versatile platform for designing organoboron compounds, and (c) lastly, boron possesses a Lewis-acidic empty p-orbital that enables coordination with lone-pair-electron-bearing ligands to form tetracoordinate boron compounds, facilitating the fine-tuning of photophysical properties (Fig. 1c).[23,24] Consequently, organoboron compounds are widely applied across fields such as organic light-emitting diodes (OLEDs),[25,26] organic field-effect transistors (OFETs),[27] organic solar cells (OSCs),[28] stimuli-responsive materials,[29] biomedicine,[30] and catalysis.[31]

Boron atoms typically act as acceptors in organoboron-based ICT molecules (OBCTs). The systematic classification of OBCTs enables a deeper understanding of boron's acceptor roles (Fig. 2a), facilitating the exploration of additional functions of boron beyond its role as an acceptor. OBCTs can be classified based on CT pathways into through-bond charge transfer (TBCT) molecules, where CT occurs *via* a π-electron bridge,[32] and through-space charge transfer (TSCT) molecules, where CT occurs directly through space.[33,34] Structurally, OBCTs are D–A or D–π–A systems, involving the transfer of π or n-electrons to the boron-containing segment. OBCTs can be further subdivided based on CT distance into long-range charge transfer (LR-CT) and short-range charge transfer (SR-CT) molecules (Fig. 2a).[35] LR-CT typically occurs in different segments involved in electron transitions, as seen in twisted intramolecular charge transfer (TICT)[36] and TSCT molecules. By contrast, SR-CT refers to charge transfer occurring within the same segment, as exemplified by multiple-resonance (MR) molecules.[37] In LR-CT molecules, strong donor–acceptor interactions can lead to long-wavelength absorption and emission, making them suitable for near-infrared (NIR) materials.[38–40] The substantial separation of FMOs also results in a small ΔE_{ST}, which is defined as the energy difference between the lowest singlet (S_1) and triplet (T_1) excited states.[41,42] However, the small ΔE_{ST} is usually accompanied by a transition-forbidden nature that could reduce oscillator strength (*f*) of transition. Additionally, drastic changes in the electronic structure increase vibrational relaxation in the excited state, broadening the emission peak and yielding a large Stokes shift. In contrast, MR molecules exhibit narrow-band and bright emission due to the alternating distribution of FMOs and a more rigid molecular framework. The moderate donor–acceptor interactions in MR molecules make them ideal candidates for blue emitters.[43–47] The combination of a locally excited (LE) state with LR-CT can be achieved in D–π–A structures, where the π-segment enhances oscillator strength and allows for a moderate ΔE_{ST}. Some molecules with this structure exhibit a hybridized local and charge-transfer (HLCT) excited-state, also known as "hot exciton" compounds,[48] which can potentially resolve the transition-forbidden issue in thermally activated delayed fluorescence (TADF). Correspondingly, hybridized multi-resonance and charge transfer (HMCT) molecules combining SR-CT with LR-CT can enhance the CT of MR molecules to achieve bathochromic-shifted emission.[49]

Finally, based on boron's coordination number, OBCTs can be classified as either three-coordinated or four-coordinated systems. Four-coordinated boron provides flexible coordination, imparting stimuli-responsive properties to the molecule.[29] However, the role of tetracoordinate boron in OBCTs remains unclear. Based on our group's recent report, this perspective systematically discusses the role of boron in tetracoordinate OBCTs, followed by a summary of two unique coordination-regulated charge transfer (CR-CT) processes (Fig. 2b): (a) coordination-enhanced charge transfer (CE-CT): boron's vacant orbitals coordinate with electron-deficient ligands while covalently bonding to donor segments. This arrangement simultaneously enhances donor and acceptor strengths, leading to red-shifted emission. (b) Coordination-quenched charge transfer (CQ-CT): this perspective further analyzes the ICT variations in

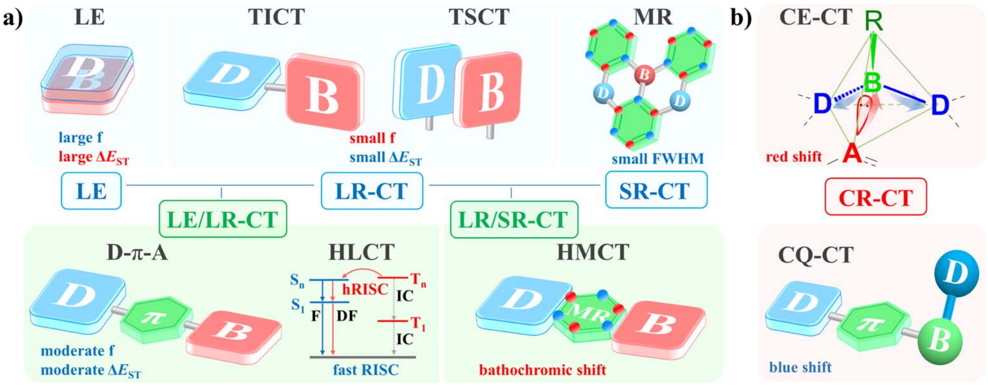

Fig. 2 Types of (a) tricoordinate and (b) tetracoordinate OBCTs.

organoboron compounds under the coordination of different ligands. For D–π–B molecules, coordination with electron-rich ligands can hinder charge transfer, resulting in the blue-shifted emission.

Extensive OBCTs have been developed around boron's unique electronic structure. However, a systematic overview of their intrinsic ICT mechanisms is still lacking, and boron's role is not limited merely to acting as an electron acceptor. This perspective provides a detailed classification of boron-dominated ICT types and reconsiders the roles of boron in organoboron molecules. Tricoordinate boron molecules are discussed in the context of TBCT and TSCT. TBCT molecules are further categorized into D–A, TICT, D–π–A, HLCT and MR systems. We discuss the fundamental principles of each process and explore their relationship. For instance, most D–A molecules rely on a π-bridge for effective CT, making them inherently D–π–A molecules. Similarly, MR molecules are actually a subset of the D–π–A molecules. Accordingly, the D–π–A molecules mentioned in this perspective are those in which π-bridges consist of alkenes or multiple aromatic rings. Unlike three-coordinated boron, four-coordinated boron acts as donor–acceptor regulator that influences molecular ICT through coordination with electron-rich or electron-deficient ligands. This perspective focuses on the emerging CE-CT and other intramolecular interactions, exhibiting significant development potential for tetracoordinate boron-domain CT compounds. The primary aim of this perspective is to summarize and analyze the ICT mechanisms in organoboron compounds, with a focus on the relationships between molecular structures and their corresponding ICT behaviors. While we include examples of both tri- and tetra-coordinated boron compounds, our selection of molecules was deliberate, chosen to illustrate specific ICT pathways and mechanisms rather than to provide a comprehensive catalog all organoboron compounds. A well-founded understanding of ICT design strategies and structure–function relationships will continue to advance design and application of OBCTs.

2. LE in organoboron compounds

LE represents an excited state without significant charge separation, predominantly occurring in π–π* transitions. The overlap of FMOs in LE ensures that electron transitions are allowed, resulting in an enhanced molecular oscillator strength when the LE fraction is increased. Direct bonding between boron and electron-rich heteroatoms (*e.g.*, N or O) is a common strategy for constructing organoboron compounds due to its synthetic simplicity and this approach also promotes electron delocalization across the entire molecule, achieving high oscillator strength.[50–57] For instance, a three-center four-electron (3c-4e) N–B–N unit provides electron-rich characteristics and high photoluminescence quantum efficiency (PLQY), where the boron p-orbital can undergo further coordination to fine-tune the optical properties.[58–60] However, the isoelectronic relationship between the C–C unit and B–N unit leads to an LE-predominated character, reducing boron's electron-accepting capacity. Similarly, integrating three-coordinated boron into electron-rich systems serves as a powerful approach to tuning optoelectronic properties of polycyclic aromatic hydrocarbons (PAHs), accompanied by weakened electron-accepting ability of boron (Fig. 3a). To achieve effective ICT with three-coordinated boron, it is advisable to avoid direct bonding between boron and heteroatoms or embedding boron into a large planar conjugated system. If direct bonding cannot be avoided, increasing the number of boron atoms or increasing the molecular twisting degree also promotes desirable CT properties, as seen in TICT-type molecules (Section 3.2).

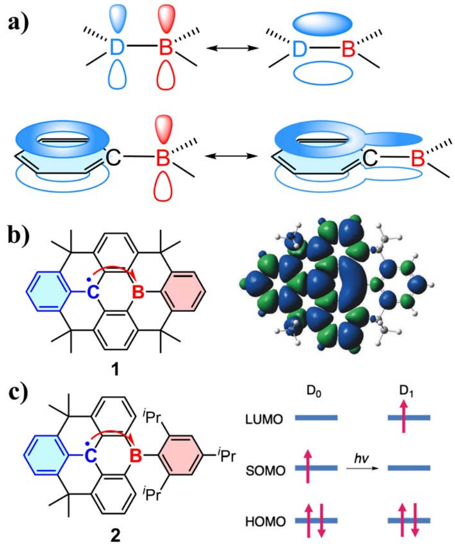

Fig. 3 (a) The p-orbitals of boron atoms filled with π-electrons in electron-rich systems *via* electron delocalization. D: electron-rich atoms (*e.g.*, N or O). (b) Stable radical **1** and its spin density distribution. Copyright 2017, American Chemical Society. (c) Stable radical **2** with a bulky boron substituent and electron transition from the SOMO to the LUMO. Copyright 2022, John Wiley & Sons. The red arrow indicates the direction of electron transition.**2**

In contrast, the presence of LE in OBCTs is not entirely detrimental. The appropriate incorporation of LE character into ICT systems can enhance molecular oscillator strength (Section 3.3) or enable highly excited-state conversion pathways such as HLCT (Section 3.4). Furthermore, the boron p-orbital can stabilize the reactive neutral carbon radical in a planar structure due to electron delocalizing properties of boron (Fig. 3b).[61] Spin density analysis of **1** indicates that the unpaired electron is efficiently delocalized over the planar molecular framework, with a significant contribution from boron. This delocalization provides compound **1** with sufficient stability for separation *via* column chromatography and the formation of single crystals detectable by X-ray diffraction. Boron also provides the LUMO for radicals **1** and **2**, enabling the rare radical electron transition from the singly occupied molecular orbital (SOMO) to the LUMO (Fig. 3c).[62] As a result, compound **1** exhibits intense red fluorescence with a high fluorescence quantum yield (Φ_F) of 0.78 in toluene.

3. TBCT in tricoordinate boron molecules

TBCT in tricoordinate boron molecules is the most extensively studied type of OBCT. We subdivide TBCT molecules into five

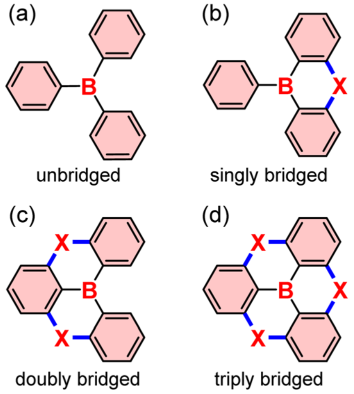

Fig. 4 (a) Unbridged, (b) single bridged, (c) doubly bridged, and (d) triply bridged triarylboryl acceptors in D–A OBCTs. X = N, O, S, CMe_2 and so on.

categories: D–A, TICT, D–π–A, HLCT and MR. For D–A molecules, we outline representative structural design strategies. TICT molecules are discussed in terms of their development and classification based on the presence or absence of rotational freedom. D–π–A molecules are categorized by their different π-bridges, while HLCT is separately discussed as a representative of D–π–A. MR molecules—recently developed and well-reviewed—are examined solely in the context of their CT process.

3.1 D–A OBCTs

Boron as an electron acceptor in D–A OBCTs can be divided into unbridged and bridged triarylboryl acceptors (Fig. 4).[23,63] The singly bridged (Fig. 4b), doubly bridged (Fig. 4c), and triply bridged (Fig. 4d) electron acceptors are common in TADF molecules and generally serve as weakened electron acceptors, which will be separately discussed in later sections. This section focuses only on the classic unbridged triarylboryl acceptors (Fig. 4a).

Triarylborane as an acceptor in D–A molecules has been extensively studied since its initial discovery in 1885 (Fig. 5).[64] To prevent nucleophilic attacks from H_2O or O_2, bulky aryl groups like 2,4,6-trimethylphenyl (Mes) or 2,4,6-triisopropylphenyl (Tipp) are often used to improve kinetic stability. Building on a prior study on photostability of dimesitylphenylborane (Mes_2BPh),[65] Williams *et al.* investigated a series of D–A type molecules with different substituents on the phenyl ring of Mes_2BPh.[66] Their findings show that *para*-positioned donor groups (*e.g.*, NMe_2 or NPh_2) on the phenyl ring of Mes_2BPh significantly increased the PLQY (88% for **3** in cyclohexane), while electron-withdrawing groups (CN or Br) result in decreased PLQYs. Additionally, the fluorescence of Mes_2BPh with electron-donating substituents exhibited a solvent-polarity-dependent red shift. This is a typical ICT process that highly polar solvents can stabilize the more polar CT state compared to the ground state, resulting in red-shifted emission. This also indicates that the introduction of D–A CT could enhance PLQY. A trigonal D–A–D molecule (**4**) with a triarylboryl core was introduced,[67] which exhibits a symmetry-broken state due to carbazole group rotation and this molecule shows a unique blue-shifted absorption sensitive to solvent polarity attributed to dipole moment inversion upon photoexcitation.

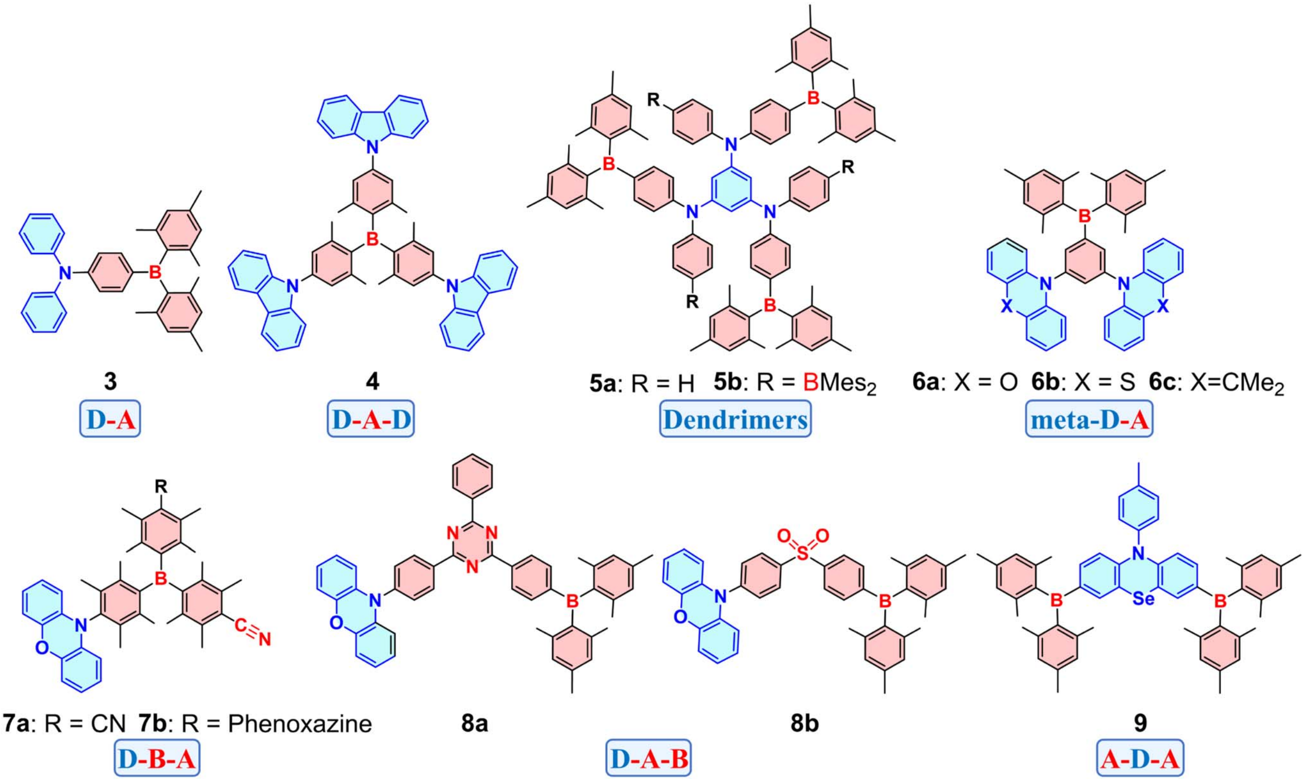

Fig. 5 Representative D–A OBCTs with unbridged triarylboryl acceptors.

Müllen *et al.* reported dendrimers **5a** and **5b** with different donor–acceptor ratios (1 : 1 and 1 : 2, respectively).[68] **5a** exhibits a 26 nm red-shifted emission and a twofold increase in concentration-dependent emission compared to **5b**. This is attributed to the additional $BMes_2$ acceptor at the *para*-position of nitrogen in **5b**, resulting in reduced nitrogen-donor strength. **5b** with six boron atoms displays a red-shifted emission upon the addition of three equivalents of fluoride, while further fluoride titration resulted in a blue-shifted emission. The former exhibits a stronger $D_{(B)}$–D–A CT due to the formation of partial B–F coordination, whereas the latter quenches the ICT process. The detailed mechanism of this phenomenon will be discussed in Section 5.2. In addition to *para*-D–A molecules, a series of *meta*-D–A molecules were reported including **6a**, **6b** and **6c** with phenoxazine (PXZ), phenothiazine (PTZ), and 9,10-dihydro-9,9-dimethylacridine (DMAC) aselectron donors, respectively.[69] The donor and acceptor units, positioned perpendicular to the central benzene ring, minimize electron delocalization and result in separated FMOs. This results in a small ΔE_{ST} value (∼30 meV). To improve the PLQY of previously reported D–A–D molecules,[70] Yang *et al.* constructed two D–B–A-type compounds, **7a** and **7b**, which showed a 5.6-fold increase (from 0.12 to 0.67) and a 1.6-fold increase (from 0.47 to 0.75) in PLQY compared to the parent D–A–D molecules.[71] These enhancements in PLQY occur despite the full charge separation in the FMOs of **7a** and **7b**. Similarly, D–A–B-type molecules using $BMes_2$ acceptors combined with triazine or sulfonyl acceptors achieve greater HOMO–LUMO separation without increasing molecular twist. **8a** and **8b** feature small ΔE_{ST} values (0.037 eV and 0.013 eV, respectively) and high PLQYs.[72] Recently, an A–D–A molecule **9** was reported to enable strong $n \rightarrow p$ or $n \rightarrow \pi^*$ transitions from N and Se atoms to two $BMes_2$ acceptors.[73] Combined with the heavy atom effect, pure green phosphorescence was observed in both the solution and doped solid film of **9** at 298 K with a PLQY of 78%. OLEDs with an external quantum efficiency (EQE) of 18.2% and a luminance of 3000 cd m^{-2} were obtained. Triarylboryl acceptors can flexibly assemble with donor units in a Lego-like manner to construct D–A OBCTs. Further tuning of the donor-to-acceptor ratio, altering arrangement patterns, and incorporating functional atoms or fragments will enable the enhancement of charge-transfer properties.

3.2 TICT OBCTs

The electron donor and acceptor units in D–A OBCTs are commonly linked through a freely rotatable single bond, enabling a conformational transformation of the molecular excited state accompanied by a dual emission phenomenon. This process is known as TICT and was first observed in 1959, when Lippert and colleagues synthesized a dye molecule **DMABN**, exhibiting dual emission peaks in solution.[74] The long-wavelength peak of **DMABN** exhibits red-shifted emission as solvent polarity increases, while the short-wavelength peak remains unaffected. The short-wavelength emission peak is believed to originate from the LE state, whereas the long-wavelength peak is due to an ICT state formed upon excitation. This ICT theory provides an initial explanation for TICT phenomenon. The unique phenomenon sparked substantial debates on the essential mechanism until Grabowski in 1973 proposed the TICT theory to explain this dual fluorescence.[75] According to the TICT theory (Fig. 6a), the TICT molecule emits from an LE/ICT state (state 2) upon excitation and then the excited molecule rotates around the single bond into a twisted conformation where the donor and acceptor are nearly perpendicular (90°) to each other. This results in a distinct TICT state (state 3) that emits fluorescence at a longer wavelength. The twisted TICT conformation is highly polar and can be stabilized in polar solvents, leading to solvent-dependent emission behaviors. Dual emission is terminated and replaced by a single emission peak when the rotation of donor or acceptor is restricted, due to limitations on excited-state structural changes (Fig. 6b). This is similar to the emission process

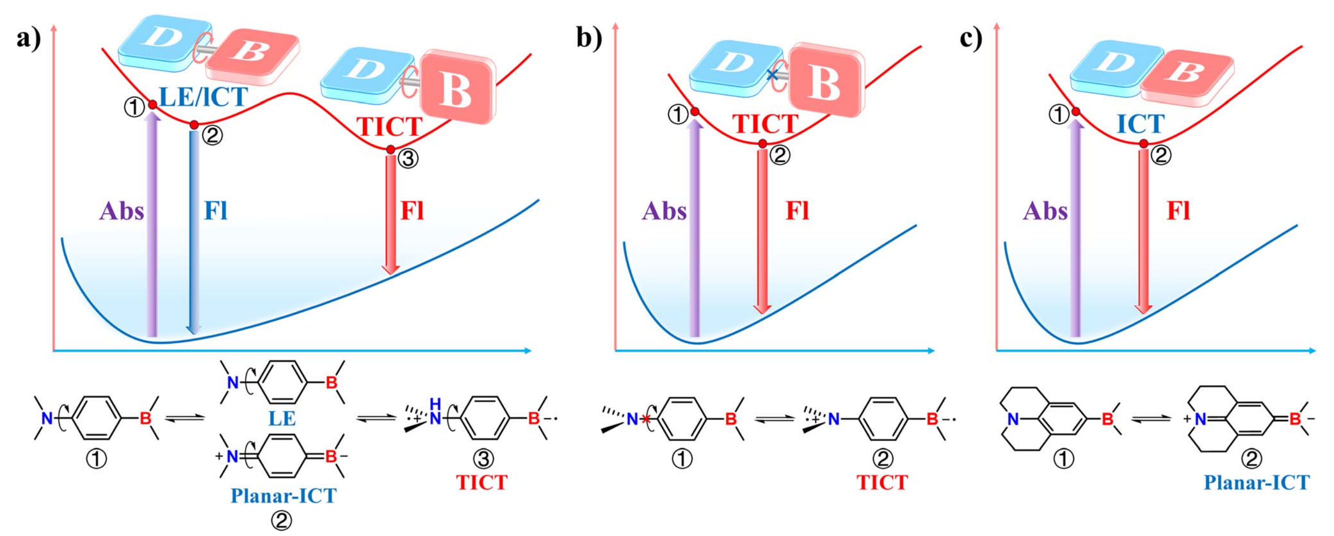

Fig. 6 (a) Dual emission in flexible TICT OBCTs. (b) Single emission in rigid TICT OBCTs. (c) ICT in planar molecules.

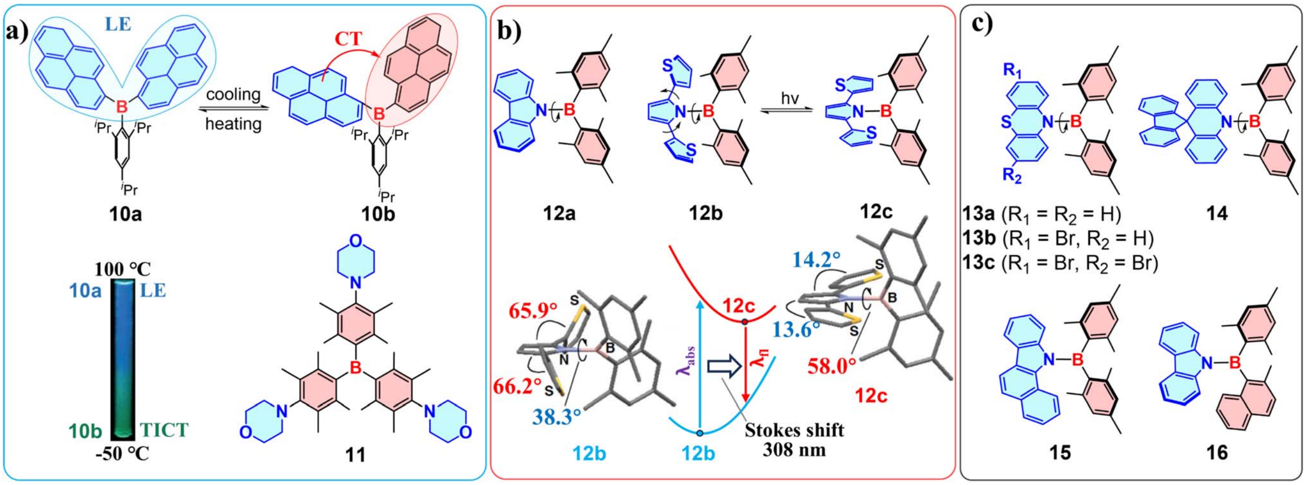

Fig. 7 Flexible TICT OBCTs. (a) Fluorescent thermometer based on temperature-dependent LE/TICT conversion and photographs showing a fluorescence color change from **10a** to **10b**. Copyright 2011, John Wiley & Sons. (b) Photo-induced TICT structural changes in OBCTs with direct B–N linkages, calculated molecular structures and fragment dihedral angles for **12b** and **12c**, and their experimental Stokes shifts. Copyright 2013, The Royal Society of Chemistry. (c) B–N linked TICT OBCTs with different donor and acceptor segments.

from a fixed-plane ICT molecule (Fig. 6c). Notably, TICT OBCTs with freely rotating donor or acceptor units (as shown in Fig. 6a) may lack dual emission. This is because two distinct excited-state conformers cannot always coexist: (1) environmental variations influence the degree of rotational freedom. For instance, temperature changes can cause one conformer to disappear entirely. (2) In some molecules, there is no energy barrier between the LE and TICT states, resulting in rapid structural relaxation of the excited state to the TICT state without any LE emission. Additionally, TICT OBCTs with twisted rigid molecular frameworks (Fig. 6b) exhibit separated FMOs, making them extensively used in TADF applications. In summary, TICT molecules are characterized by a twisted excited-state molecular structure and can be classified as flexible and rigid TICT systems depending on the flexibility of single-bond rotation.

Flexible TICT OBCTs undergo significant structural changes upon excitation, resulting in large Stokes shifts (Fig. 7). Yang and colleagues reported a fluorescent thermometer (**10a**/**10b**) operating over a temperature range of −50 °C to 100 °C (Fig. 7a).[76] The pyrene segments in **10a** enable flexible rotation at higher temperatures, which favors blue emission from the LE-state. In contrast, the rotation becomes restricted at lower temperatures, leading to a twisted conformation **10b** that features TICT-state green emission. This finding highlights the significant impact of temperature on the LE to TICT emission ratio. Later, they introduced another D–A–D-type temperature indicator **11** that displayed temperature-driven LE and TICT transitions in both liquid solvents and solid-state polymers.[77]

The weakened D–A strength arising from direct B–N bonding can be restored in TICT molecules. Aminoborane TICT molecules **12a** and **12b** with direct B–N linkage were reported (Fig. 7b).[78] **12a** demonstrates a substantial increase in BN bond twisting upon excitation, with the corresponding dihedral angle increasing from 28.6° to 62.4°. **12b** features flexible rotation around both the thiophene–pyrrole and B–N bonds, exhibiting a 308 nm Stokes shift in THF (absorption maximum at 349 nm and fluorescence at 657 nm). The thiophene–pyrrole segment in S_1 of **12b** becomes nearly planar while the BN fragment further twists upon excitation, which enhances donor strength and forms a TICT state. Ghosh and colleagues described another series of phenothiazine-based TICT OBCTs **13a–13c** with direct B–N bonding (Fig. 7c), which exhibit large Stokes shifts (up to 312 nm), aggregation-induced emission (AIE), and mechano-fluorochromism upon grinding.[79] The mechanoluminescence in these compounds is ascribed to the flexible phenothiazine structure. Spiro-functionalized acridine as a donor was used to further enhance FMO separation in aminoboranes, resulting in the development of first *N*-borylated emitters **14** with TADF. A green OLED device based on **14** exhibits an EQE of 19.2%.[80] Subsequently, methoxy-substituted carbazoles as donors were exploited to achieve efficient blue *N*-borylated emitters.[81] π-Conjugation extensions in both the carbazole (**15**)[82] and the mesityl of the boron group (**16**)[83] were also investigated. It was found that extending the donor enhanced π-conjugation and steric hindrance, resulting in a red-shifted emission and a smaller Stokes shift in **15**.[82] Compound **16** exhibits solvatochromism in its emission spectra, with its emission peak shifting from 448 nm in hexane to 495 nm in acetonitrile. It also shows circularly polarized luminescence (CPL) with a dissymmetry factor (g_{lum}) of approximately 3×10^{-4} due to its axial chirality.[83]

Rigid TICT molecules are frequently utilized in achieving TADF (Fig. 8). Adachi reported the first boron-substituted TADF molecules **17** with phenoxaborin as the acceptor.[84] The dimethylacridine donor and boron acceptor of **17** are almost orthogonal (89.61°), resulting in excellent FMO separation (Fig. 8a) with a ΔE_{ST} of 0.10 eV and enabling a blue OLED with a high EQE of 21.7%. Among structurally similar D–A molecules, **18a** and **18b**, the dihedral angles between the phenylene bridge and the donors differ greatly (54.7° in **18a** *versus* 88.9° in

18b) due to the smaller steric hindrance of the carbazole donor in **18a** (Fig. 8b). As a result, only **18b** displays TADF with a ΔE_{ST} of 0.013 eV, whereas **18a** shows no TADF with a ΔE_{ST} of 0.35 eV.[85] This indicates that large steric hindrance between the donor and acceptor is crucial for effectively separating the FMOs, thereby achieving TADF in rigid TICT OBCTs. Compound **19** with a blocked triarylborane acceptor, also exhibits TADF behavior due to its near-orthogonal donor–acceptor dihedral angle (87.3°), leading to a green OLED based on **19** with 22.8% EQE.[86] Incorporation of a boron-sulfur unit into molecule **20** increases the rate of reverse intersystem crossing (RISC) through enhancing spin–orbit coupling (SOC), thereby shortening the TADF lifetime to $\approx 1\ \mu s$.[87] In addition, **20** with a donor–acceptor torsion angles of 87.1° restricts relaxation from S_1 to the ground state (S_0), producing a narrow full-width at half-maximum (FWHM) of 0.32 eV and enabling TADF-OLEDs based on **20** to achieve a maximum external quantum efficiency (η_{ext}) of 25.3% at 503 nm. Adjusting donor components can further achieve efficient blue TADF-OLEDs.[88,89]

Doping more than one boron atom into molecules can enhance TADF performance. Cheng and co-workers reported twisted D–A–D configuration molecules, **21a** and **21b**, with borylanthracene as the acceptor.[90] This arrangement effectively separates FMOs, resulting in small ΔE_{ST} values of 22–33 meV and achieving up to 37.8% EQE with small efficiency roll-off featuring only a 3%drop at 1000 cd m^{-2} for green OLEDs. π-Extended ladder-type oxaborin and thiaborin acceptors have been exploited to construct **22a** and **22b**.[91] Introducing sulfur atoms endows compound **22b** with a k_{RISC} that is 3.5 times higher than that of **22a** ($8.8 \times 10^{-6}\ s^{-1}$ *vs.* $2.5 \times 10^{-6}\ s^{-1}$). NTO analyses and SOC matrix element calculations reveal that RISC occurs from the locally excited T_2 state rather than T_1 to the charge-transfer S_1 state (Fig. 8c). Furthermore, $\langle S_1|\hat{H}_{SO}|T_2\rangle$ of **22b** is over 30 times larger than that of **22a** ($2.93\ cm^{-1}$ *vs.* $0.09\ cm^{-1}$), attributed to the heavy-atom effect of sulfur. The combination of acridine derivatives as donors and highly hindered triarylborane as the central acceptor has been used to construct star-shaped blue TADF emitters.[92] Upon replacing the donor with a dimethylacridine derivative, a star-shaped molecule achieved 38.8% EQE.[93] TICT molecule **23** achieved yellow TADF-OLED emission at 556 nm, owing to its B-heterotriangulene acceptors bearing electron-deficient carbonyl groups that lower the LUMO level (Fig. 8d).[94] OLEDs based on **23** exhibit very low efficiency roll-off, achieving a maximum EQE of 28.4% and maintaining EQEs of 21.5% at 5000 cd m^{-2} and 17.7% at 10 000 cd m^{-2}. Replacing the carbonyl group with an electron-rich oxygen atom yields weaker acceptors, resulting in blue TADF.[63] A linear D–A molecule **24** was synthesized by Wang *et al.*, featuring a weak spiro-donor and spiro-acceptor separated by a bulky π-spacer.[95] The rigid framework enables an OLED doped with **24** (30 wt% in mCBP) to exhibit high-purity emission at 444 nm with CIEy < 0.06. This deep-blue device also shows great resistance to efficiency roll-off, achieving a maximum EQE of 25.4% and retaining 20.0% at 1000 cd m^{-2}. Recently, TICT molecules **25** with a rigid structure exhibiting a small ΔE_{ST} of 0.1 eVenabled a sky-blue OLED with 32.6% EQE.[96] Compared to the extensively studied TICT molecules with *para*-positioned acceptors and donors, molecules with *meta*-positioned triarylboryl acceptors have also been used to fabricate TADF-OLEDs.[97]

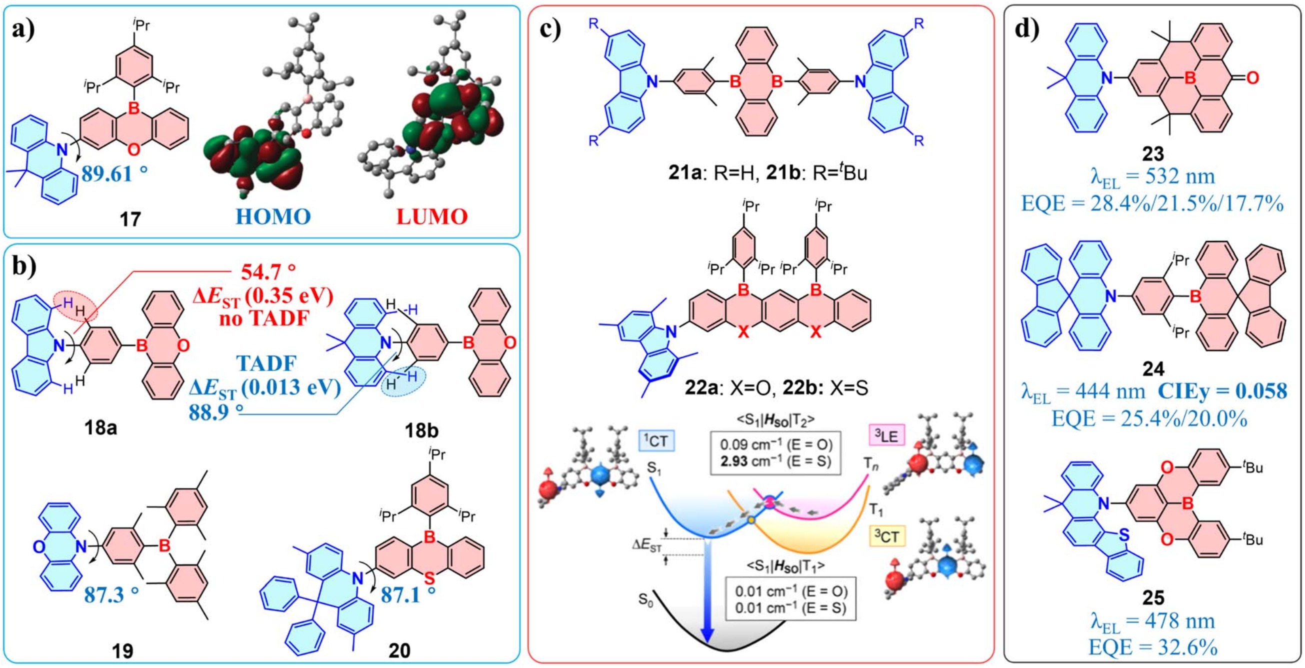

Fig. 8 Rigid TICT OBCTs with TADF properties. (a) Classic TICT boron-based TADF molecule and its FMO distribution. Copyright 2015, The Royal Society of Chemistry. (b) TADF TICT OBCTs affected by donor–acceptor steric hindrance. (c) Dual-boron-doped TADF TICT OBCTs and a schematic representation of the spin-converting RISC mechanism induced by SOC for **22a** and **22b**. Copyright 2020, American Chemical Society. (d) TICT TADF OBCTs with different boron acceptors and their corresponding TADF-OLED performance.

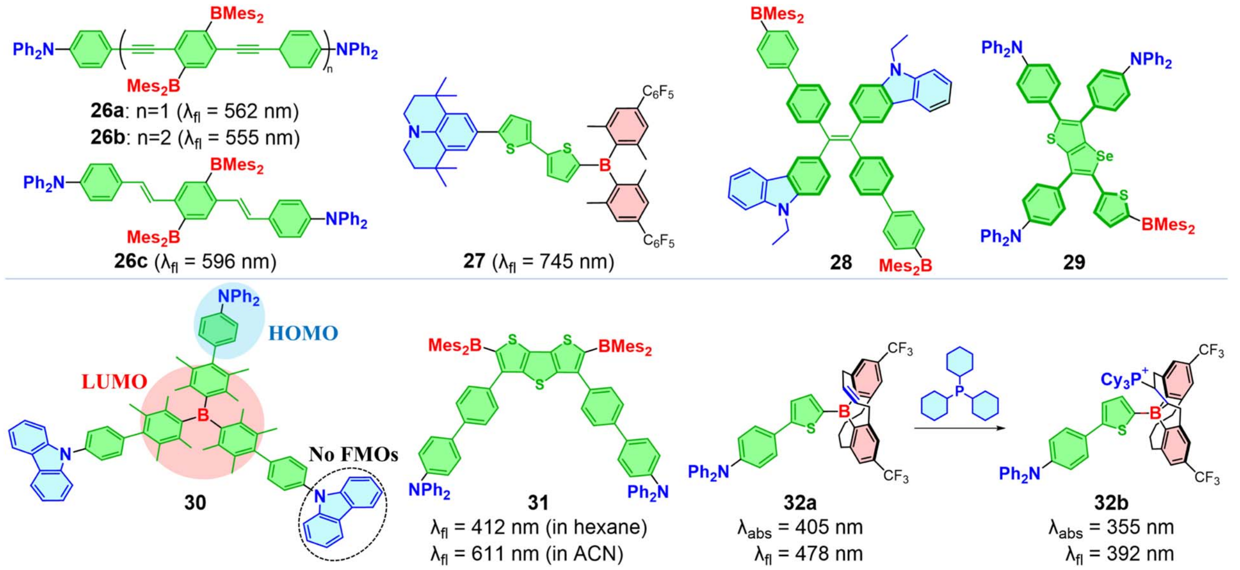

Fig. 9 D–π–A OBCTs with linked aromatic π-bridges.

3.3 D–π–A OBCTs

D–π–A OBCTs can be divided into two categories: those with single bond linked (Fig. 9 and 10) and fused aromatic (Fig. 11 and 12) π-bridges. Additionally, single bond linked D–π–A OBCTs including macrocyclic and pillar[5]arene D–π–A OBCTs are also included in this section (Fig. 10). Numerous linear D–π–A OBCTs have been developed since the first D–π–A OBCTs reported by Williams *et al.* in 1972.[66] Shirota reported boron-containing linear D–π–A molecules with a thiophene π-

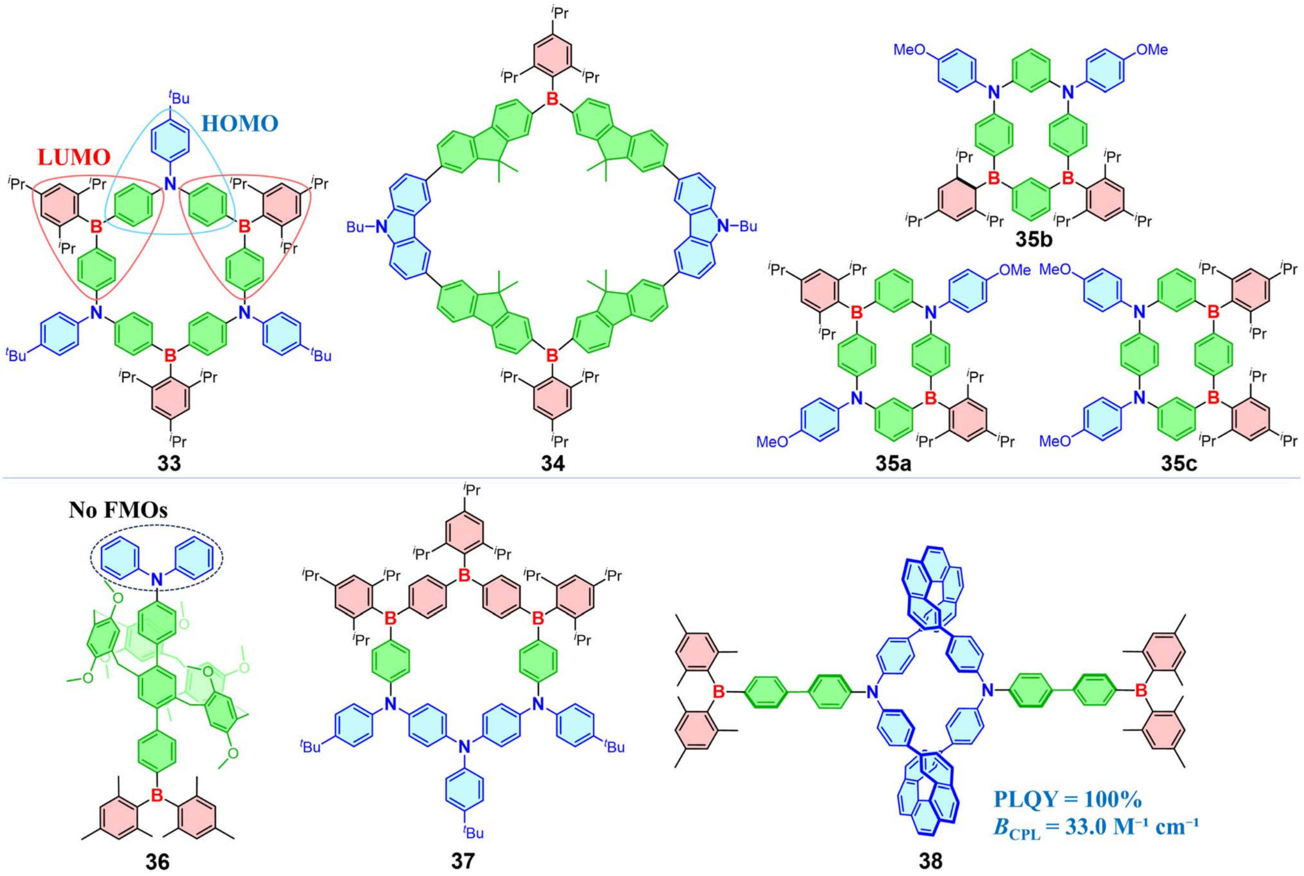

Fig. 10 Macrocyclic and pillar[5]arene D–π–A OBCTs.

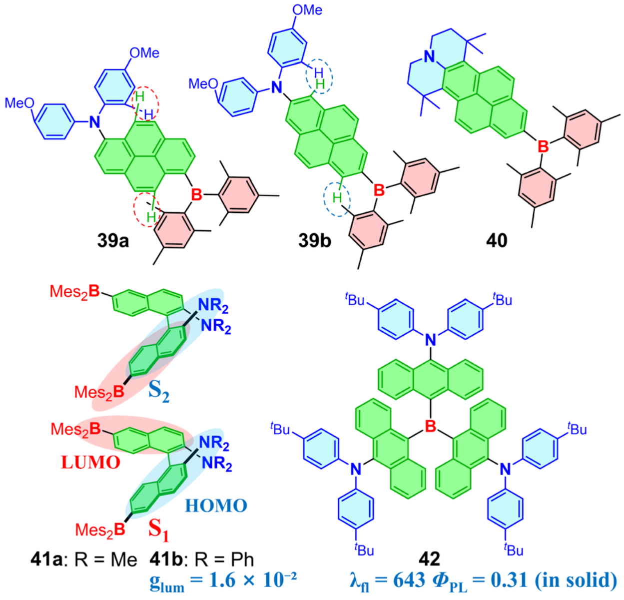

Fig. 11 D–π–A OBCTs with fused aromatic π-bridges.

bridge, fabricating blue-green and green OLEDs.[98] In contrast to linear D–π–A configurations, non-linear D–π–A molecules (**26a–26c**) that incorporate boryl groups as side chains exhibit twisted molecular geometries and intense solid-state fluorescence in films.[99] **26a** displays a more intense red-shifted fluorescence than **26b** (562 nm, $\Phi_F = 0.90$ *vs.* 555 nm, $\Phi_F = 0.86$) in films, while an ethenylbenzene π-bridge in compound **26c** enables a further red-shifted emission up to 596 nm ($\Phi_F = 0.73$). These observations imply that regulating π-bridges can achieve red–NIR light emissions by influencing the CT process. Marder's team combined a dithienyl π-bridge and a strong donor–acceptor pair to obtain compound **27**, which exhibited near-infrared (NIR) emission at 745 nm with a PLQY of 48% in acetonitrile. This is the first example of a three-coordinated organoboron compound showing efficient NIR emission.[100] Subsequently, D–π–A molecules with unsymmetrically substituted triarylboryl acceptors were developed.[101] This indicates that steric hindrance from substituents on boron could prevent the excited-state from becoming planar, thereby enhancing the molecules' photostability.

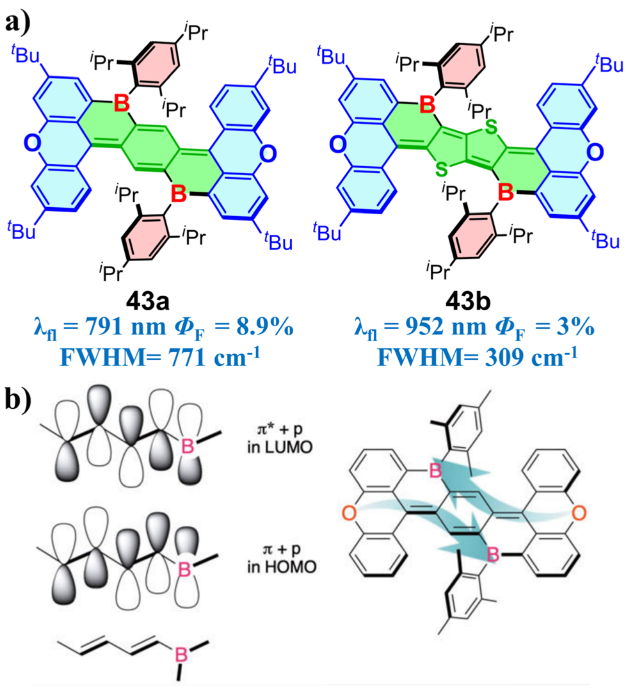

Fig. 12 (a) NIR emissive OBCTs with fused aromatic π-bridges based on an electron push–pull effect. (b) Illustration showing the orbital interaction of FMOs and the push–pull effect in **43a**. Copyright 2021, John Wiley & Sons.

Introducing the tetraphenylethene (TPA) π-bridge and the TPA-like fused selenophenothiophene π-bridge into D–π–A OBCTs affords compounds **28** (ref. 102) and **29**,[103] respectively, both of which exhibit notable TICT-driven solvatochromism and AIE behavior. Star-shaped D–π–A molecule **30** with asymmetric architecture, has the HOMO primarily concentrated on the more electron-rich diphenylamine segment, enabling blue phosphorescent OLEDs.[104] In fact, ICT primarily occurs on fragments comprising the strongest donor and acceptor parts in molecules. Ozturk presented a D–π–A molecule with a fused thiophene π-bridge, exhibiting a 200 nm solvent-dependent red shift (412 nm in hexane to 611 nm in acetonitrile).[105] Recently, Yamaguchi introduced olefin-borane acceptors to construct D–π–A molecule **32a**, which exhibited pronounced solvatochromism.[106] The unique olefin structure in **32a** allows the C═C double bond to weakly coordinate with boron. The addition of a Lewis base to **32a** triggers frustrated Lewis pair (FLP)-type interactions and forms **32b** rather than direct coordination with the boron atom, resulting in significantly altered absorption and emission properties.

Design strategies of D–π–A are also applied in constructing macrocyclic and pillar[5]arene OBCTs (Fig. 10). In 2012, Jäkle introduced the seminar ambipolar macrocycle with a boron–π–nitrogen (B–π–N) structure (**33**), exhibiting intense blue fluorescence.[107] Notably, the HOMO of **33** only distributed across one of the nitrogen donors and bridging phenylene rings, while the LUMO primarily localizes on two boron acceptors adjacent to the nitrogen donor where the HOMO is located, with minor contributions from the exocyclic phenyl rings. Additionally, macrocycle **34** with fluorene as the π-bridge exhibits significant D–π–A transitions, with the overlapping region of FMOs located on the fluorene moiety. Consequently, molecule **34** displays a pronounced bathochromic shift as the solvent polarity increases.[108] Among B–π–N-embedded cyclophanes, **35a–35c**, the arrangement of **35c** exhibits the smallest HOMO–LUMO gap and clearly separated FMOs, resulting in fluorescence quenching of the S_1 state.[109] Interestingly, **35a** exhibits a red-shifted emission and a rise in Φ_F from 0.16 to 0.40 with increasing solvent polarity, which violates the energy-gap law as opposed to compound **35b**. Incorporating a B–π–N structure into pillar[5]arenes achieves a PLQY of 99% in solution and a PLQY of 57% in solid for **36**, compared to parent pillar[5]arenes with low PLQY (<0.01).[110] Notably, DFT calculations indicate that the

HOMO responsible for the S_1 transition of **36** localizes on the pillar[5]arene structure instead of nitrogen, because the electron-donating effect of the methoxy group allows the pillar[5]arene framework to act as a donor. Compound **37** exhibits a red-shifted emission at 612 nm compared to **33**, where the donor and acceptor of **37** are spatially separated on opposite sides of a π-extended ring system.[111] Further exploration examines the impact of low symmetry and the B/N ratio on CT, which indicates that single-boron macrocycles exhibit stronger CT properties and smaller HOMO–LUMO energy gaps than their highly symmetric aza/boracyclophane analogues.[112] Chen *et al.* synthesized organoborane macrocycles **38** using chiral [5] helicenes combined with a B–π–N structure, which displayed strong emissions with PLQYs of up to 100% in solution and 34% in solid.[113] The CPL brightness ($B_{\mathrm{CPL}} = \varepsilon \times \Phi_{\mathrm{PL}} \times g_{\mathrm{lum}}/2$) of the figure-of-eight macrocycle **38** is 33.0 $\mathrm{M^{-1}\,cm^{-1}}$, ranking among the highest values reported for [*n*]helicene-based small organic molecules at that time. Introducing boron atoms to tailor charge transfer in macrocyclic molecules is an efficient strategy for significantly boosting their luminescence performance.

As one of the representative fused aromatic π-bridges, pyrene was used to construct OBCTs **39a** and **39b** (Fig. 11).[114] **39a** exhibits a more twisted structure than **39b** due to larger steric hindrance between donor/acceptor and pyrene in **39a**. This results in a more red-shifted solvatochromism for **39a**, with a maximum emission at 658 nm in acetone. Notably, **39b** shows an increase in PLQY from 0.07 to 0.36 as the emission shifts from 458 nm in *n*-hexane to 561 nm in CH_2Cl_2, which obeys the energy-gap law. Similarly structured molecule **40** with a fixed electron donor exhibits a high radiative transition rate.[115] Axially chiral D–π–A molecules **41a** and **41b** were reported with naphthalene as the π-bridge.[116] Compound **41a** exhibits dual emissions of 485 nm and 535 nm at 20 °C. Upon heating, the intensity of the short-wavelength emission peak increases rapidly, whereas upon cooling from 20 °C to −50 °C, the long-wavelength emission peak originating from the CT state undergoes a 31 nm bathochromic shift. The transition of S_1 is from the dimethylaminonaphthyl group of one D–π–A subunit to the LUMO on the dimesitylborylnaphthyl moiety of other subunit, while S_2, responsible for short-wavelength emission, primarily involves transitions within the same subunit (Fig. 11). **41b** exhibits an intense CPL response, achieving tunable CPL properties *via* fluoride titration and a high luminescence g_{lum} of 1.6×10^{-2}. Compared to the star-shaped D–π–A OBCTs, molecules **42** with bulky 9,10-anthrylene as the π-bridge shows a pronounced D–π–A transition from the anthrylamine moiety to the anthrylborane moiety.[117] The large steric hindrance of the π-bridge in **42** imparts significant resistance to aggregation-caused quenching (ACQ), exhibiting solid-state emission at 643 nm with a PLQY of 31%.

In addition, Yamaguchi introduced a push–pull effect by fusing an aromatic π-bridge with boron to generate narrow NIR emitting materials **43a** and **43b** (Fig. 12a).[118] **43a** exhibits a narrow emission at 791 nm, with a Stokes shift of 21 nm (345 $\mathrm{cm^{-1}}$), a FWHM of 49 nm (771 $\mathrm{cm^{-1}}$), and a PLQY of 8.9%. The crystal structure of **43a** reveals a quinone-like π-bridge that facilitates conjugation between the empty p-orbital on boron and the π/π* orbitals of the butadiene structure (Fig. 12b). This arrangement enables an effective electron push–pull interaction between boron and the distal diphenyl ether donor, resulting in NIR emission. Furthermore, replacing the central benzene with an electron-rich thienothiophene unit yields compound **43b**, which exhibits an even narrower NIR emission at 952 nm, with a Stokes shift of 7 nm (78 $\mathrm{cm^{-1}}$), a FWHM of 28 nm (309 $\mathrm{cm^{-1}}$) and a PLQY of 3%. Integrating boron-dominated CT with a fused aromatic π-bridge is an effective strategy for inducing red-shifted emission in tricoordinate boron systems, particularly enabling near-infrared emission.

3.4 HLCT OBCTs

In addition to the typical upconversion from T_1 to S_1, reverse intersystem crossing (RISC) can also occur between higher triplet states (T_m, $m > 1$) and singlet states (S_n, $n \geq 1$), a process known as high-lying reverse intersystem crossing (hRISC).[48,119] This can be achieved by HLCT molecules that feature a hybrid LE state and CT state, ensuring a high radiative decay rate from S_1 to S_0 and facilitating hRISC from T_n to S_n.[120,121] HLCT molecules enable efficient triplet exciton utilization and typically possess a D–π–A structure. Boron-based receptors, which readily introduce LE character, are ideal for constructing HLCT molecules. However, HLCT OBCTs have been relatively less reported (Fig. 13).

Introducing cyano groups to modify the triarylborane acceptor endows **44** with strong electron-accepting characteristics (Fig. 13).[122] It exhibits oxygen-sensitive PLQYs and delayed fluorescence phenomena. Lower temperatures result in shortened prompt fluorescence decay and lengthened delayed fluorescence decay for **44**, probably due to the hot-exciton process. The weakened boron acceptor, such as **DOBNA**, is more common in HLCT OBCTs in order to ensure a higher LE ratio. **45** was constructed by combining **DOBNA** as a weak acceptor and anthracene as a weak donor.[123] The LE state in compound **45** is located on the central anthracene unit, whereas the CT state occurs from the anthracene to **DOBNA**. A significant ΔE_{ST} of 1.33 eV was observed for **45** while the S_1/S_2 and T_4/T_5 energy levels were very close, promoting efficient hRISC processes. Devices doped with compound **45**exhibit deep-blue emissions with a maximum EQE of 10.1%. Recently, Yan and co-workers reported a structurally similar HLCT OBCT, based on which a non-doped device achieved deep-blue emission with minimal efficiency roll-off, from an EQE of 8.4% at 1000 cd $\mathrm{m^{-2}}$ to 5.14% at 10 899 cd $\mathrm{m^{-2}}$.[124] D–π–A molecule **46**, which exhibits near ultraviolet (UV) emission at 414 nm, was generated by incorporating **DOBNA** and tetrahedral tetraphenylsilane (TPS) with large steric hindrance, featuring a LE state located on **DOBNA** and a CT process occurring from **DOBNA** to the phenyl rings of TPS.[125] Additionally, **46** exhibits a 0.52 eV energy gap between the S_1 and T_1 states while the energy gap between S_1 and T_3 is only 0.04 eV, indicating the HLCT properties of **46.** Yang *et al.* exploited fluorene as the π-bridge to construct a D–π–A molecule, **47**.[126] Weak hybridization is observed between the S_2 and S_1 states of **47**, wherein a high PLQY is achieved *via* an LE-like HLCT S_1 with higher oscillator strength, while a "hot-exciton"

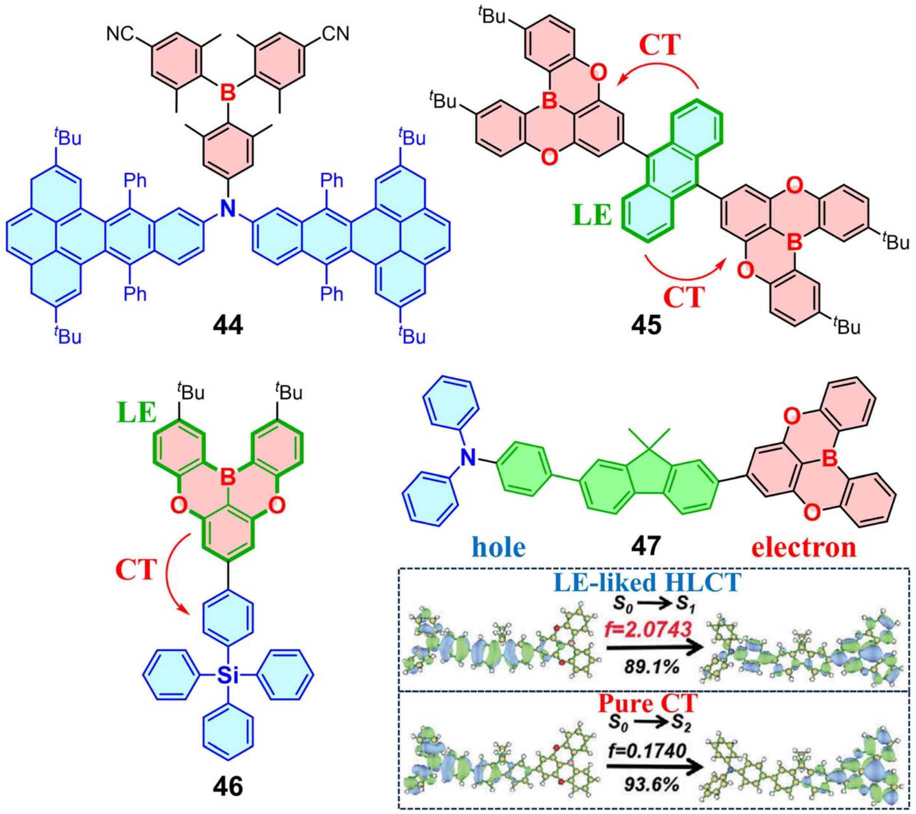

Fig. 13 HLCT OBCTs. The inset shows $S_0 \rightarrow S_1$ and $S_0 \rightarrow S_2$ NTO analysis of **47**. Copyright 2024, John Wiley & Sons.

channel is primarily formed from the nearly pure CT S_2 state (Fig. 13). DFT calculations further indicate that hRISC occurs between S_1 and T_6 as well as between S_2 and T_5 in **47**.

Weak boron acceptors can facilitate an effective HLCT process with short-wavelength emission. Double BO-embedded PAHs **48a** and **48b** exhibit narrow UV and violet-blue emission (FWHMs of 25 and 37 nm, respectively) in toluene, where the directly bonded B–O atoms act as weak acceptors, imparting the molecules with LE-dominated HLCT properties (Fig. 14a).[127] TD-DFT calculations of **48a** and **48b** reveal that S_1 has small energy gaps and large SOC matrix elements with T_3–T_6, whereas it exhibits opposite characteristics with T_1 (Fig. 14b). This suggests the efficient utilization of hot excitons *via* hRISC processes, as evidenced by oxygen-sensitive PLQYs. The **48a**- and **48b**-based UV and UV-blue OLEDs exhibit both high color purity and high efficiency. In particular, the **48a** device features emission at 394 nm, with a CIEy of 0.021, a FWHM of 48 nm, and a EQE of 11.3%, making it one of the best performing UV OLEDs reported with CIEy < 0.05.

3.5 MR OBCTs

LR-CT involves substantial vibrational relaxation processes in the excited state, resulting in broadened emissions and reduced PLQYs in TADF molecules. In 2016, Hatakeyama and co-workers introduced the SR-CT mechanism of MR-TADF, utilizing the opposing resonance effects of boron and nitrogen atoms to achieve an alternant HOMO/LUMO arrangement in the central phenyl ring (Fig. 15a).[128] The efficient separation of FMOs enables a small ΔE_{ST} with TADF characteristics while minimizing excited-state electron-structure changes. Additionally, the rigid framework decreases reorganization energy, leading to a narrow FWHM and high PLQY. Two classic MR-TADF molecules named **DOBNA**[128] and **DABNA**[37] have been successively reported. Furthermore, Duan[129] and Wang[130] developed a carbazole-based molecule **49**, featuring a more rigid structure and red-shifted emission (Fig. 15b). Boron-based MR-TADF molecules have made rapid progress in recent years and have been systematically summarized.[131–133] Therefore, this section focuses on strategies for tuning MR-TADF properties involving CT.

Most of the MR-TADF molecules emit exclusively in the blue to green region. By expanding the framework of **49** based on carbazole and its derivatives, Yasuda *et al.* synthesized MR-TADF OBCTs **50a** and **50b** with opposite shifts in emission wavelength.[134] **50a** with *para*-arranged B–π–N units displays a blue-shifted emission due to weakened D–A interactions, while **50b** with *para*-arranged B–π–B and N–π–N units produces red emission at 615 nm due to strengthened D–A interactions (Fig. 15c). This strategy of combining B–π–B and N–π–N is widely applied to achieve longer-wavelength emission for MR-TADF molecules.[132,135] Additionally, the non-bonding nature of MR-TADF which limits conjugation expansion is generally accepted as a factor restricting the red shift of emission for MR-TADF molecules.[136] Considering that donor–acceptor strengths

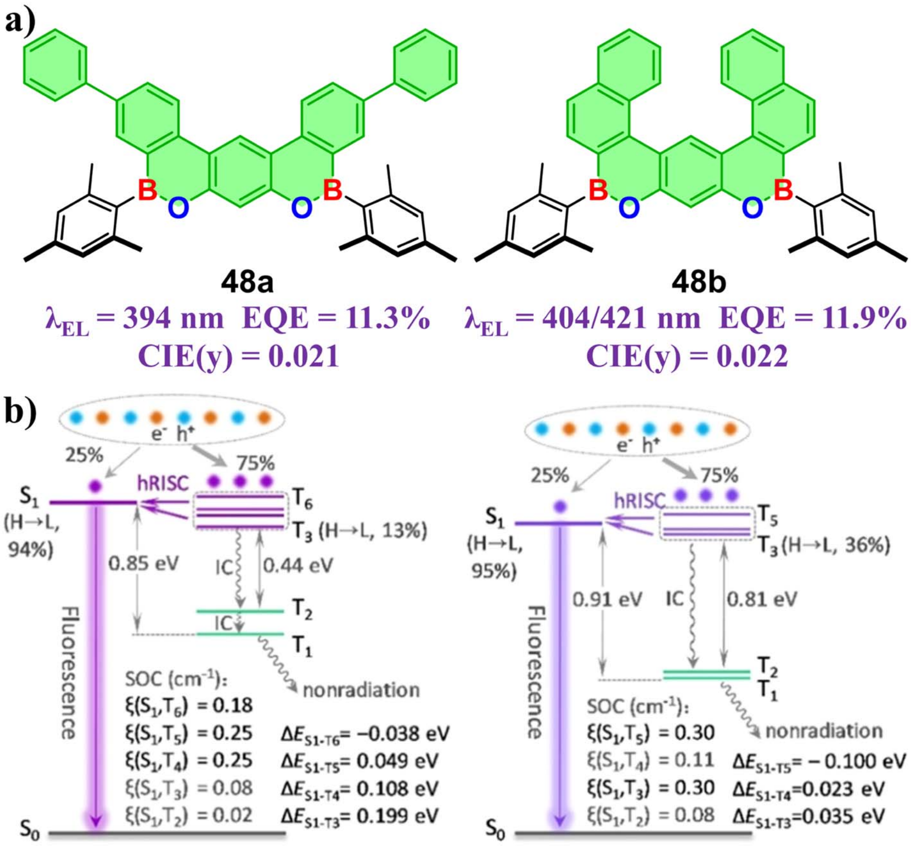

Fig. 14 (a) HLCT OBCTs with a directly bonded B–O atom acceptor, and their corresponding OLED performances. (b) TD-DFT-calculated singlet and triplet energy levels, along with SOC matrix elements between S_1 and T_n states, for **48a** and **48b**. Copyright 2024, American Chemical Society.

directly affect the energy gap of molecular transitions, the influence of different MR-arrangements on donor–acceptor interactions are discussed as follows.

As shown in Fig. 15d, the *ortho* D–π–B configuration facilitates charge separation within the central phenyl ring, resulting in a smaller ΔE_{ST}. However, opposite resonance and inductive effects between the donor and boron mutually weaken their strengths. Similarly, in the *para*-D–π–B configuration, donor–acceptor strengths are diminished without an inductive effect. Therefore, MR-TADF essentially involves a weak CT process. For *meta*-B–π–B/D–π–D structures, the opposite resonance effects that act on the same atoms of phenyl ring strengthen the MR in OBCTs. When these configurations are combined, they are expected to yield blue-shifted TADF emission. In contrast, the *para*-B–π–B/D–π–D configurations, in which the same resonance effects alternately locate on the central phenyl ring against MR effects, result in enhanced donor or acceptor strength. Similar influences on the donor or acceptor are observed in the *ortho*-B–π–B/D–π–D configuration, while an additional inductive effect further enhances donor or acceptor strength. In the *meta*-D–π–B configuration, opposite resonance effects on the same atoms of the central phenyl ring cancel each other out and increase the ΔE_{ST} of the molecules. MR-TADF molecules with these two configurations are anticipated to exhibit red-shifted emission, in which the central phenyl ring shows π–π* LE characteristic.

Integrating the MR effect with LR-CT also enables red-shifted emissions (Fig. 16). Duan *et al.* introduced electron-withdrawing substituents at the *para*-position of the boron-attached benzene ring in **49** to generate molecules **51**. The LUMO of **51** extends onto the fluorophenyl substituent, conferring CT characteristics and resulting in blue-green TADF at 494–499 nm.[129] Then, the concept of HMCT was proposed to construct molecule **52** by extending the π system with an electron-withdrawing aza-phenanthrene moiety.[49] The enhanced ICT character of **52** reduces the HOMO–LUMO energy gap, leading to a sharp green emission at 522 nm (FWHM = 28 nm) and an extremely high PLQY of 99.7%.

Applying the HMCT strategy into D–π–A systems formed the hybrid LR/SR-CT molecule **53**, in which D-MR-A design resulted in a high oscillator strength with a smaller ΔE_{ST}.[35] In addition, symmetric **DOBNA** units on both sides of **53** exhibit dual CT pathways, doubling the oscillator strength (from 0.1426 to 0.3498) compared to the molecule with single-sided **DOBNA** and achieving an OLED with a high EQE of 40.4%. Recently, Hatakeyama and co-workers developed a donor/acceptor "core–shell" molecule **54** by introducing an additional boron atom into a deep-blue MR matrix.[137] The highly localized tri-boron region with a strong electron-withdrawing effect effectively deepens the

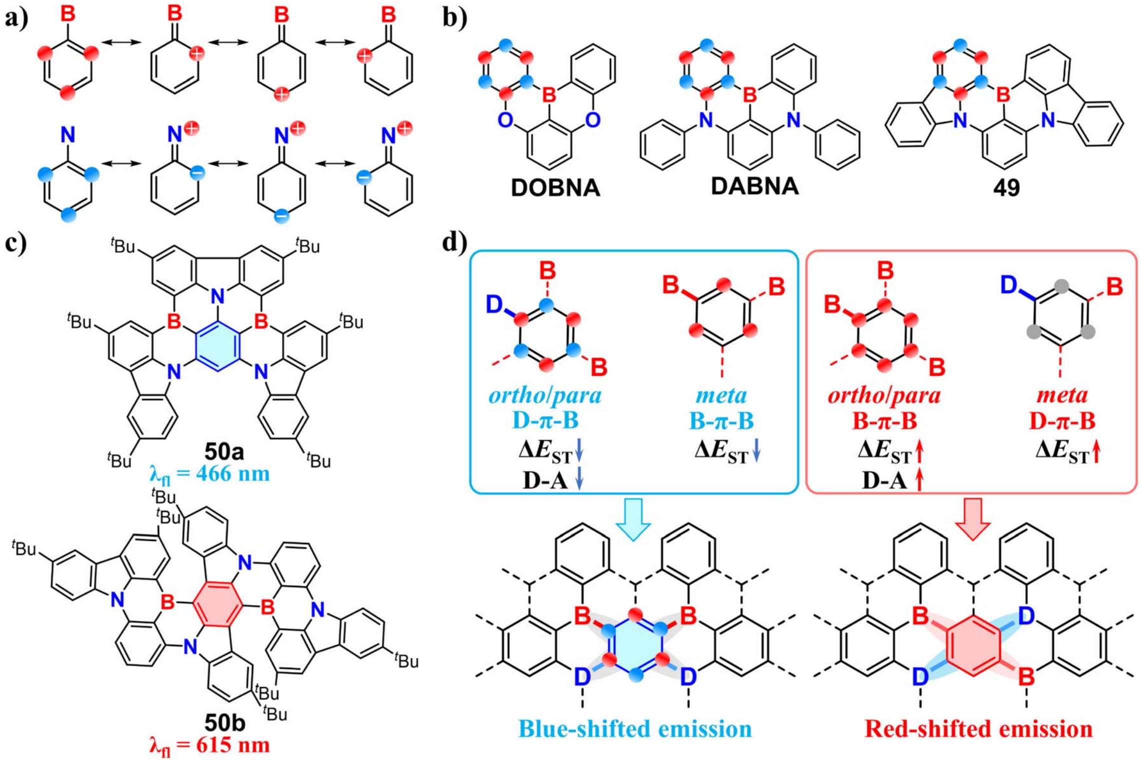

Fig. 15 (a) MR-TADF design principles. (b) Representative MR-TADF OBCT structures. (c) B–π–B and N–π–N structures reported by Yasuda. (d) Effects of atomic arrangements on ΔE_{ST} and donor–acceptor characteristics of MR-TADF molecules.

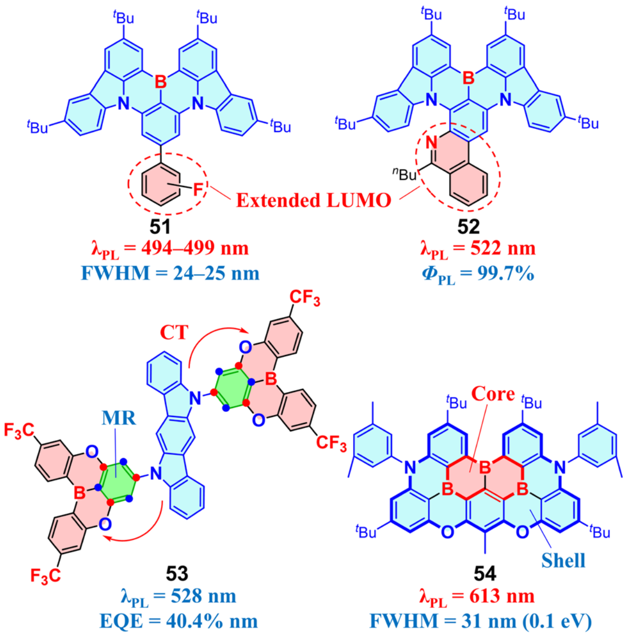

Fig. 16 TADF molecules utilizing hybrid LR/SR-CT.

LUMO level, inducing LR-CT between the B core and electron-donating MR shell fragments in the rigid structure. As a result, compound **54** exhibits an emission at 613 nm with a narrow FWHM of 31 nm, representing a 172 nm red shift compared to the MR-matrix shell compound. The **54**-based OLEDs achieve pure-red emission up to 624 nm with an EQE of 23.3% and demonstrate excellent electroluminescence stability, with a maximum LT_{99} (time to 99% of the initial luminance) exceeding 400 h at an initial luminance of 1000 cd m^{-2}.

4. TSCT in tricoordinate boron molecules

TSCT occurs in π-stacked systems where two or more aromatic units are close but not covalently bonded.[33,34] TSCT OBCTs can be classified based on the type of π-spacer: rotatable and fused. A single-bond-connected spacer is rotatable with greater flexibility, enabling parallel D–A configurations (Fig. 17), while a fused π-spacer imparts rigidity to molecule frameworks, which is ideal for constructing TSCT TADF emitters (Fig. 18–20).

In 2006, Wang and colleagues reported the first TSCT OBCT **55** where the donor N(Ph)(1-naphthyl) and acceptor $BMes_2$ are linked to rotatable biphenyl groups bridged by a naphthalene unit.[138] The U-shaped geometry of **55** allows TSCT from the amine to the boron unit, which can be blocked by fluoride titration, resulting in a fluorescence change from green to brighter blue (Fig. 17a), serving as a "turn-on" sensor for fluoride. Subsequently, V-shaped TSCT molecule **56** with an organosilicon spacer was developed, offering increased rotational freedom between donor and acceptor groups and increased sensitivity to fluoride.[139] Introduction of a dimethylarylamine donor created a TSCT molecule featuring a similar structure to

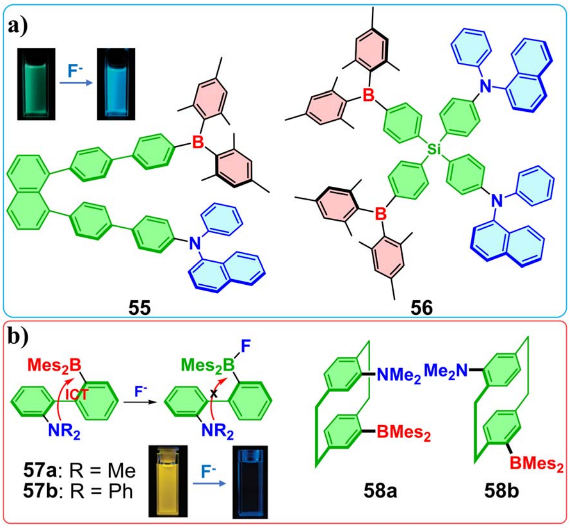

Fig. 17 (a) U-shaped and V-shaped TSCT OBCTs with a rotatable π-spacer. Insets showing the fluorescence change of **55** before and after fluoride titration. Copyright 2006, John Wiley & Sons. (b) TSCT OBCTs with a smaller spacer. Insets showing the fluorescence change ofr **57a** before and after fluoride titration. Copyright 2011, American Chemical Society.

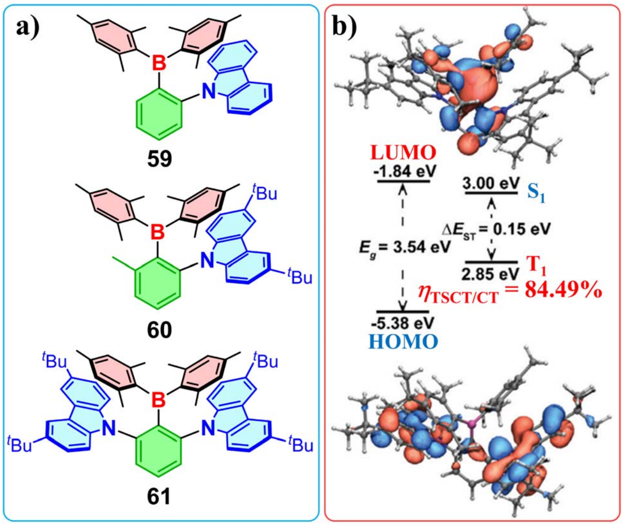

Fig. 18 (a) TADF-emissive TSCT molecules with triarylboron acceptors. (b) The calculated HOMO/LUMO distributions, ΔE_{ST} and the TSCT/CT ratio ($\eta_{TSCT/CT}$) for **61**. Copyright 2021, The Royal Society of Chemistry.

55 and dual responsiveness to fluoride and protons, in which fluorescence shifts to sky blue upon fluoride titration while protonation of the amine shifts emission to purple.[140] A smaller spacer can also be applied to construct TSCT molecules. A rotatable biphenyl spacer was used to construct molecules **57a** and **57b** with $BMes_2$ and NPh_2 at adjacent positions. These molecules exhibit bright TSCT fluorescence and undergo significant blue shifts upon fluoride titration due to the inhibition of the ICT process (Fig. 17b).[141] Then, they introduced a new family of triarylborane-based [2,2]paracyclophane derivatives **58a** and **58b**, enabling efficient TSCT fluorescence and TADF.[142] Remarkably, the enantiomerically pure form of **58a** exhibits strong CPL with a g_{lum} of up to 4.24×10^{-3}.

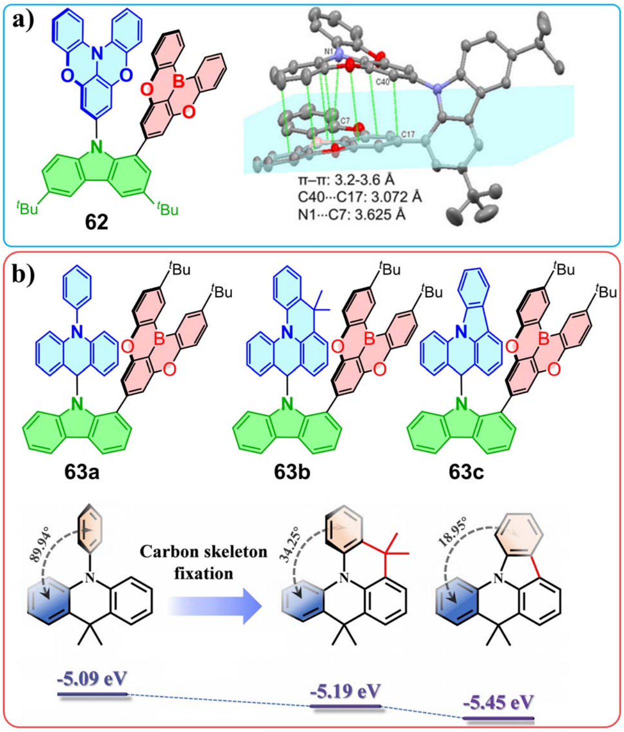

Fig. 19 (a) TSCT OBCTs with a planar donor and **DOBNA** acceptor in a face-to-face orientation. Single crystal structure of **62** showing the strong intramolecular π–π interactions. Copyright 2020, John Wiley & Sons. (b) TSCT OBCTs with different skeleton-modified phenyl acridine donors, as well as the relationship between structures and HOMO levels of phenyl acridine and its derivatives based on DFT calculations. Copyright 2022, John Wiley & Sons.

The twisted TSCT structures can effectively separates FMOs and avoid ACQ of emission (Fig. 18a), which have been widely utilized in designing efficient TADF emitters. The TSCT molecules with TADF are typically constructed by arranging the donor and acceptor at adjacent positions on the fused π-spacer. This can shorten the π–π interaction distance between the donor and acceptor, resulting in an enhanced transition dipole moment and reduced vibrational relaxation. The bulky triarylboron acceptors can improve molecular rigidity of TSCT OBCTs to enhance TADF performance. Compound **59** with a $BMes_2$ acceptor has intrinsic steric "locking" that enables a highly twisted conformation, resulting in a small ΔE_{ST} of 0.15 eV and an efficient blue TADF at 463 nm.[143] The electron-donating groups substituted at boron's *para* position of **59** induce a blue shift in emission,[144] while electron-withdrawing groups cause a red shift.[145] The highly separated HOMO and LUMO of **60** are localized primarily on the carbazole and $BMes_2$ units, respectively, indicating that charge transfer occurs through both the aryl linker and through space. This dual-mode CT gives rise to a small ΔE_{ST} of 0.05 eV alongside a large transition dipole moment.[146] Moreover, the twisted framework of **60**

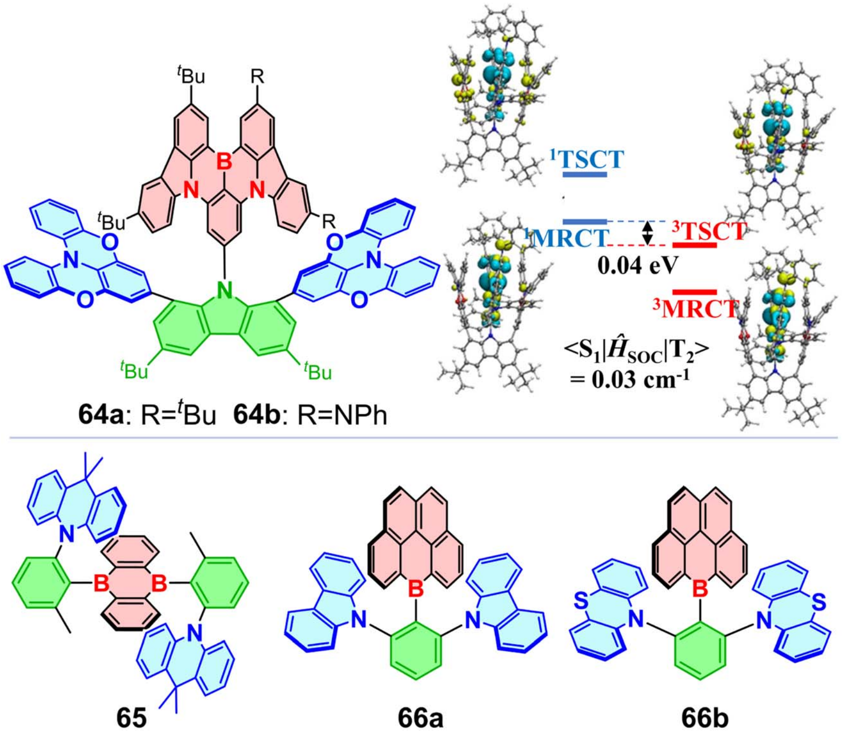

Fig. 20 TSCT OBCTs with different planar boron acceptors. The illustration showing calculated hole (green) and electron (blue) distributions and energy gaps of the ^{1,3}MRCT and ^{1,3}TSCT excited states for **64b**. Copyright 2023, John Wiley & Sons.

effectively suppresses intermolecular π–π stacking, enabling blue non-doped OLEDs to achieve an exceptional EQE of 19.1%. *ortho*-D–A–D TSCT OBCT **61** features distinct CT from two carbazole units to the triarylboryl unit (Fig. 18b).[147] NTO analysis of the hole–particle overlap reveals that TSCT contributes up to 84.49% of the total CT character. The OLEDs incorporating **61** exhibit green electroluminescence with a maximum EQE of 27.5%.

Planar MR boron acceptors, such as **DOBNA**, are also widely used for constructing TSCT OBCTs with TADF properties, which require larger fused aromatic rings as spacers. Yang *et al.* employed *tert*-butyl carbazole as a rigid spacer to build the TSCT molecule **62**, where the planar donor and **DOBNA** acceptor exhibited strong intramolecular π–π interactions in a face-to-face orientation (Fig. 19a).[148] This increases the radiative decay rate of S_1 and suppresses non-radiative decay, resulting in a PLQY up to 0.99 in thin films doped with **62**. A device with 30 wt% of **62** achieves maximum EQE/current efficiency/power efficiency values of 23.96%/76.74 cd A^{-1}/65.63 lm W^{-1}, respectively. A TSCT dendrimer with blue TADF characteristics was developed by incorporating three **DOBNA** acceptors. The CT process in this dendrimer mainly arises from TSCT, with intrafragment charge transfer (IFCT) analysis revealing a contribution ratio of 92.2%.[149] Gradual planar skeleton modification of phenyl acridine from **63a** through **63b** to **63c** leads to progressively closer intermolecular donor–acceptor stacking, which diminishes vibrational relaxation and produces increasingly narrow FWHMs from 57 nm to 35 nm (Fig. 19b). **63a** and **63b** show ultrapure-blue TADF, while **63c** exhibits a large ΔE_{ST} of 0.29 eV without TADF due to the weak carbazole donor strength.[150] Notably, introducing an additional *tert*-butylcarbazole substituent at the *para* position of carbazole in **63c** induced TADF emission by enhancing the carbazole donor strength, reducing ΔE_{ST} to 0.09 eV.[151]

The MR segment **DABNA** can also act as an acceptor to construct TSCT OBCTs (Fig. 20). **64a** and **64b** display a sandwiched structure, with the **DABNA** acceptor playing dual roles as both a TADF emitter and an electron acceptor.[152] The RISC process of **64b** occurs from the TSCT-type T_2 to the MR-type S_1, with a large SOC matrix element $\langle ^1\mathrm{MRCT}|\hat{H}_{\mathrm{SOC}}|^3\mathrm{TSCT}\rangle$ of 0.33 cm^{-1} (Fig. 20), resulting in fast delayed fluorescence with a lifetime of 10.6 μs. A 3 wt% doped device with **64b** reaches a maximum EQE of 31.7%. Recently, Xiao and co-workers combined MR and TSCT strategies to design a high-performance green narrowband OLED, achieving an EQE of 32.3%.[153] Another planar 9,10-diboraanthracene acceptor was used to construct **65**, which exhibited strong red TADF and produced a red OLED with an EQE of 10.1% at 615 nm.[154] In addition, molecules **66a** and **66b** were obtained using a highly planar benzene-fused boracycle.[155] The distance between B and N in **66a** and **66b** decreases when the donor is switched from carbazole to electron-rich phenothiazine, indicating stronger π–π interactions between the boron acceptor and phenothiazine. Notably, **66a** exhibits no TADF properties, likely due to the weak carbazole donor. These compounds display low PLQYs in solution and high PLQYs at low temperatures or in doped thin films.

5. ICT in tetracoordinate boron molecules

Tetracoordinate boron molecules with sp^3 hybridized boron atom exhibit a stable and blocky octet electron configuration compared to tricoordinate boron molecules, forming a three-dimensional architecture with ACQ resistance.[26,156] Additionally, the three-dimensional form also allows greater flexibility in designing tetracoordinate boron compounds. In terms of electronic properties, the filled p-orbital in tetracoordinate boron eliminates its electron-withdrawing capability, giving it a distinctly different role in the CT process compared to tricoordinate boron. To date, research on the CT mechanism of tetracoordinate boron compounds is still relatively limited. This section provides an in-depth analysis of the roles of tetracoordinate boron in the CT process.

5.1 Chelation of tetracoordinate boron

Tetracoordinate boron is commonly exploited as an acceptor fragment in charge-transfer molecules, which can be categorized into four types based on the chelated donor atoms: *O*,*O*-chelate, *N*,*C*-chelate, *N*,*O*-chelate, and *N*,*N*-chelate (Fig. 21a).[157] Strong electron-withdrawing groups like F, CF_3, and C_6F_5 are usually incorporated into these compounds as substituents of boron. Understanding the impact of chelation at the tetracoordinate boron center on the ICT process is crucial for advancing the design of functional tetracoordinate compounds.

Liu and co-workers analyzed single-crystal structures of BODIPY and observed that the two B–N bonds in the N–B–N unit had equivalent bond lengths of approximately 1.55 Å, suggesting the existence of a resonance hybrid involving both B–N and B→N bonding (Fig. 21b). Accordingly, a novel tetracoordinate boron molecule **67** was developed to exhibit a resonance hybrid of N–B–N bonds.[158] The single-crystal structure of **67** reveals similar B–N bond lengths (around 1.54–1.55 Å), despite the two nitrogen atoms in the N–B–N unit differing in their chemical environments. Notably, the HOMO distribution of **67** is skewed toward the dihydrophenazine moiety, while the LUMO is slightly preferentially localized on the thiazole segment. This is likely due to the influence of more dominant resonance forms on FMOs. Furthermore, molecules **68a** and **68b** were synthesized, featuring a hyperconjugation effect that influences the electronic structure and stabilizes different redox states (Fig. 21c).[159] This highlights that σ–π hyperconjugation can occur in tetracoordinate boron compounds without disrupting conjugation, thus facilitating the CT process. The covalent and coordination bond lengths were measured to be 1.56 and 1.64 Å in the single crystal of **68a**, respectively, indicating that bulky phenyl substituents on boron lengthen the B–N bonds and weaken the coordination bond, resulting in a reduced resonance effect.

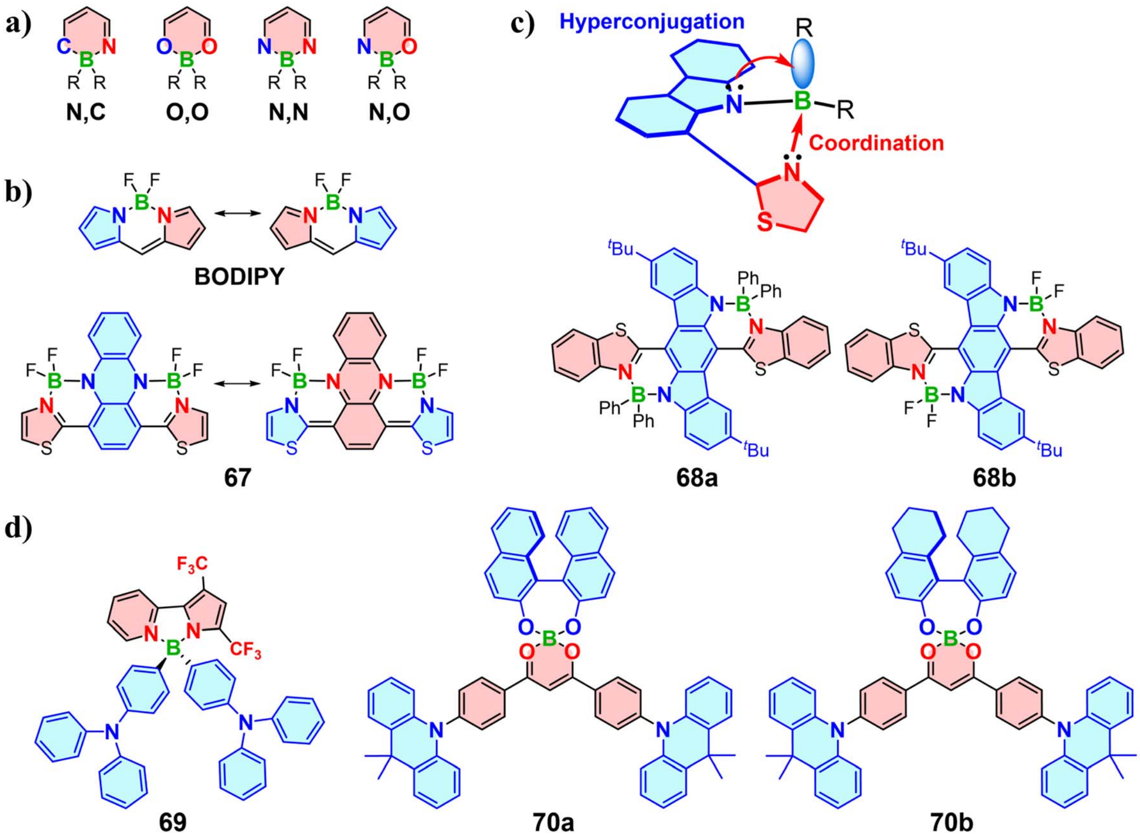

Fig. 21 (a) Chelation types of tetracoordinate boron as an acceptor fragment. (b) Resonance hybrid involving B–N and B→N bonding (c). Hyperconjugation effect in the tetracoordinate boron molecules. (d) Tetracoordinate boron TADF molecules.

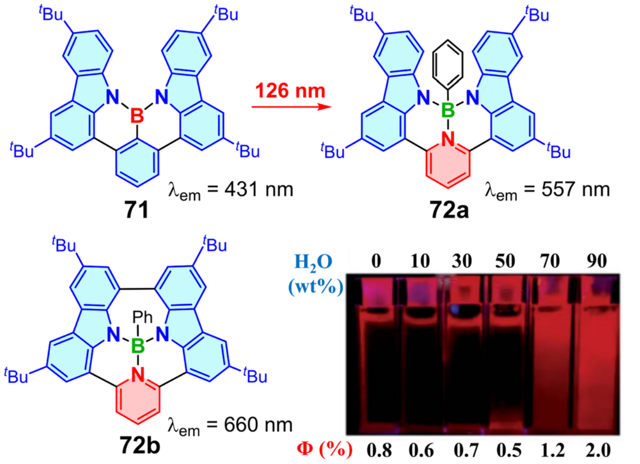

Fig. 22 Tri- and tetra-coordinate boron molecules with NBN fragments and their maximum emission wavelengths in 10^{-5} M THF solution. The inset shows the photograph showing the emission intensity increase of **72b** with the increasing H_2O fraction. Copyright 2022, The Royal Society of Chemistry.

Chou *et al.* utilized tetracoordinate boron as the linkage unit to generate molecule **69**, which revealed that the HOMO and LUMO were well-separated and that tetracoordinate boron contributed to a rigid molecular framework (Fig. 21d).[160] They subsequently fabricated the first TADF OLED based on tetracoordinate boron molecule **69**, achieving a maximum EQE of 13.5%. Recently, spirocyclic NIR emitters **70a** and **70b** were introduced by incorporating a tetracoordinate boron acceptor, a dimethylacridine (DMAC) substituent and either chiral binaphthol, or octahydro-binaphthol donors.[161] The LUMOs of **70a** and **70b** are primarily localized on the acceptor unit of the β-diketone-coordinated boron and the adjacent benzene ring, indicating a robust OBO resonance effect, while the HOMOs exhibit different distributions depending on the electron-donating strength of the chiral units. Solution-processed, non-doped OLEDs based on these emitters show NIR emission peaking at 716 nm, with a maximum EQE of 1.9% and a high exciton utilization efficiency of 86%.

5.2 Coordination-enhanced/quenched charge transfer

The thriving development of OBCTs has been closely linked to the innovative exploration of the CT process. In contrast to the well-established π-acceptor roles of tricoordinate OBCTs, tetracoordinate boron compounds with a filled p-orbital present a conundrum regarding clarification of their underlying CT process, an understanding of which will facilitate the diverse advancement of tetracoordinate boron OBCTs. In 2022, our group reported a tetracoordinate boron compound **72a**, featuring intriguing TADF properties.[162] Compared to its parent tricoordinate boron molecule **71**,[163] **72a** exhibits a red-shifted emission exceeding 100 nm, reaching 557 nm. In addition, **72b** with a fused heptagon displays a deep-red emission at 660 nm and shows significant AIE behavior (Fig. 22).

Recently, we constructed a family of tetracoordinate boron-based twisted helicenes **73a–73d**, achieving red-shifted emission with narrower FWHM by combining an alternating D–π–A framework with boron-induced CE-CT (Fig. 23).[164] **73a–73d** designed using the CE-CT strategy, utilize the electron-withdrawing pyridine ligand to coordinate with the empty p-orbital of boron, enhancing the pyridine acceptor strength. The four-coordinated boron atom in **73a–73d** features low electronegativity and an electron-octet structure, which pushes σ-electrons to the carbazole donor fragments. The boron atom in the CE-CT process serves as a bridge for the electron shuttling, resulting in a push–pull effect with enhanced CT. In addition, these compounds display red-shifted emissions up to

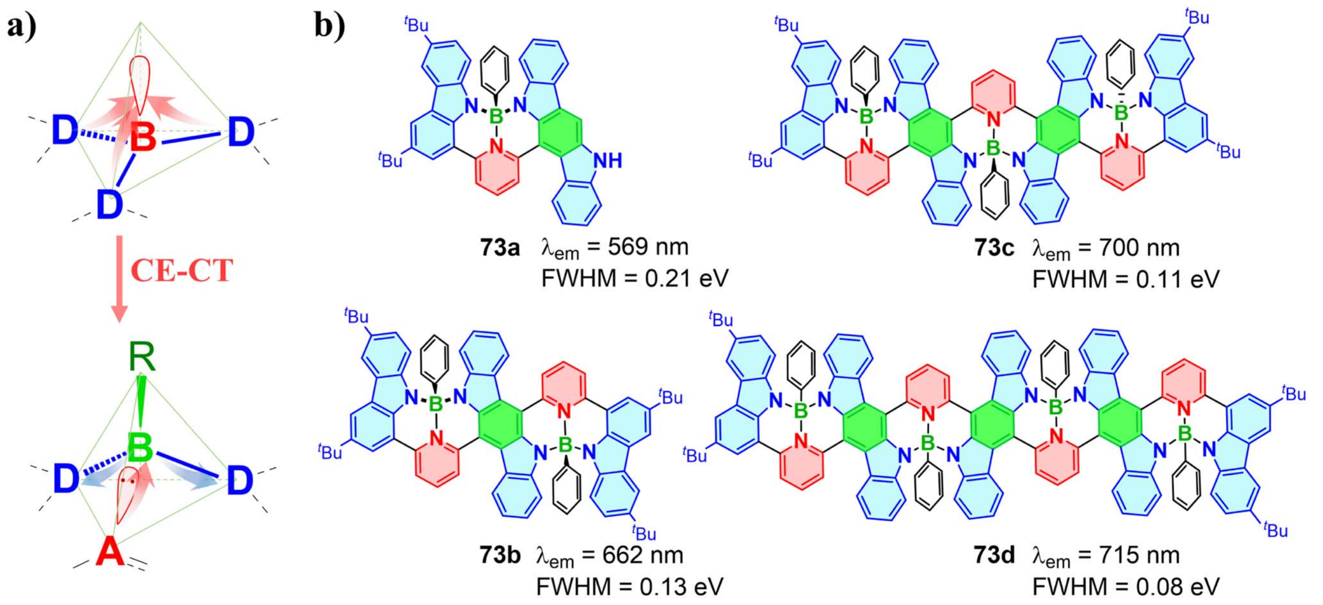

Fig. 23 (a) Coordination-enhanced charge transfer mechanism. Copyright 2024, John Wiley & Sons. (b) A family of tetracoordinate boron helicenes and their maximum emission wavelengths and FWHMs in 10^{-5} M toluene solution.

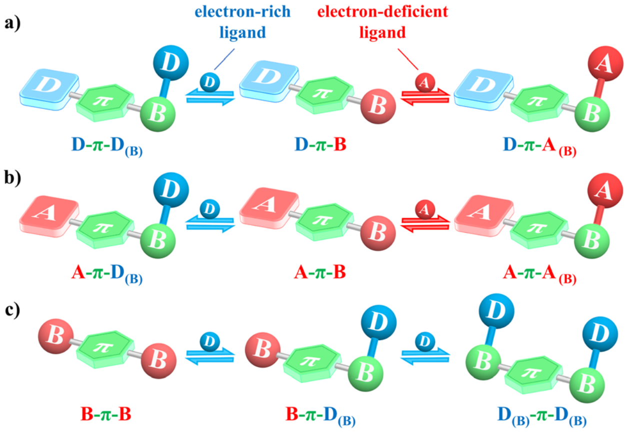

Fig. 24 The effect of coordination on the CT process of (a) D–π–B, (b) A–π–B and (c) B–π–B systems, D: electron-donor, A: electro-acceptor, and B: boron atom.

753 nm at higher concentrations. *Cis*/*trans* configurational isomers of **73c** were separated and exhibit nearly identical photophysical properties. Subsequently, IFCT and Huang–Rhys factor calculations clarified the phenomenon of narrowing red-shifted emission. The CE-CT strategy offers a solution to the challenge of achieving red-shifted emission in OBCTs.

Inspiringly, the principle of CE-CT can also elucidate the effect of coordination on the CT process of tricoordinate boron compounds. Different ligands could lead to opposite CT effects during the coordination process, in which the ligands can be categorized into two types: (1) electron-rich donor-type ligands, which include various anions like fluoride and saturated amine groups such as NMe_2 and NPh_2, and (2) electron-deficient acceptor-type ligands, including heteroaromatics (*e.g.*, pyridine and benzothiadiazole) and carbonyl (*e.g.*, ketone and aldehyde). Two tricoordinate boron theoretical models are proposed in this perspective, D–π–B and A–π–B systems, to investigate the impact of coordination with different ligands on CT process, aided by in-depth analysis of CE-CT (Fig. 24). Coordination with an electron-rich ligand in the D–π–B system will reduce the electron-donor ability of the ligand and form a D–π–$D_{(B)}$ system, which commonly exhibits an enlarged energy gap due to the $D_{(B)}$-quenched CT process (Fig. 24a). Notably, weak $D_{(B)}$ usually does not participate in FMOs and the above process can be termed as coordination-quenched charge transfer (CQ-CT). During this process, coordination with an electron-rich ligand inverts the original boron acceptor into a weak donor unit ($D_{(B)}$), so CQ-CT can also be termed acceptor-inversion coordination-quenched charge transfer (iCQ-CT). The proposed CQ-CT has several potential applications: (1) the change in emission properties upon coordination with specific

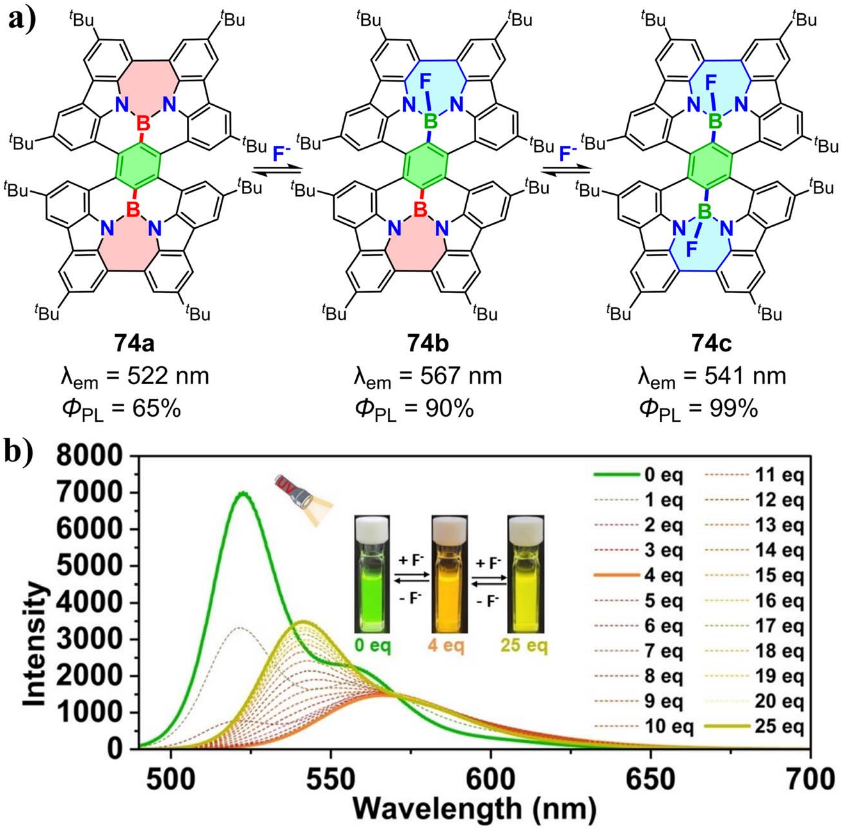

Fig. 25 (a) Double-fluoride titration of double-boron doped helicene **74a**. (b) Titration experiments of **74a** in acetone (1.0 × 10^{-5} M) solution with TBAF, measured using fluorescence spectra (λ_{ex} = 470 nm). Inset: photographs showing fluorescence of **74a** with 0 equiv., 4.00 equiv. and 25 equiv. of TBAF in acetone. Copyright 2023, John Wiley & Sons.

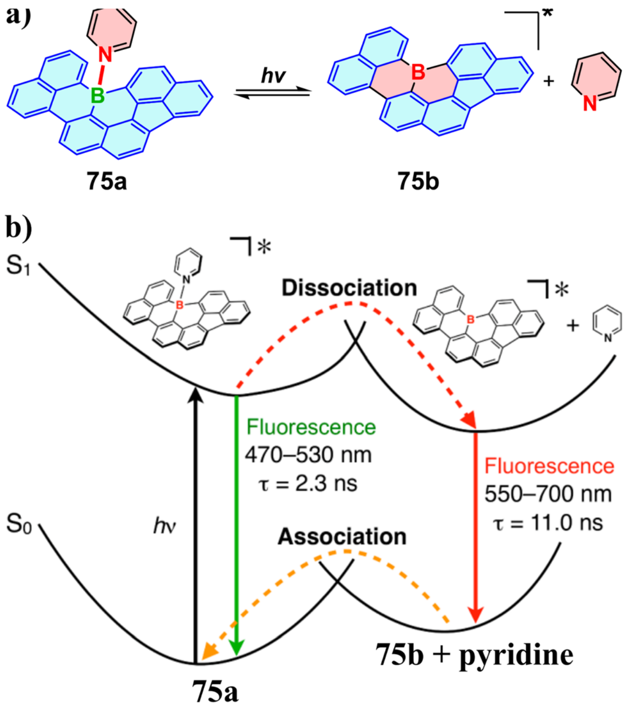

Fig. 26 (a) Photoinduced coordination cleavage of triarylborane–pyridine complex **75a**. (b) A plausible energy diagram for the photodissociation process. Copyright 2014, American Chemical Society.

ligands can be exploited for sensing applications. For instance, the quenching of emission in response to the presence of certain anions or biomolecules can serve as a selective and sensitive detection mechanism. This can be particularly useful in biological sensing, where the detection of specific ions or molecules is crucial. (2) CQ-CT can be utilized to design switchable materials whose optical properties can be modulated by external stimuli. By controlling the coordination environment, one can switch between states with different emissive properties, which can be applied in smart windows, displays, and other optoelectronic devices that require dynamic control of light transmission or emission. (3) In energy transfer systems, CQ-CT can be used to regulate the efficiency of energy transfer. By designing systems where the charge transfer is quenched upon coordination, one can control the flow of energy in a molecular circuit, which can be beneficial in solar cells and other photovoltaic applications.

In contrast, the D–π–B system coordinating with an electron-deficient ligand could enhance electron-acceptor ability of the ligand and form a new D–π–$A_{(B)}$ system, resulting in a red-shifted absorption and emission if the new CT is stronger than that of the D–π–B system (Fig. 24a). This process involves CE-CT similar to that in **73a–73d**. In the A–π–B system, coordination with an electron-rich ligand forms an A–π–$D_{(B)}$ system, which typically enhances molecular CT and leads to a red-shifted emission due to the generated D–π–A architecture (Fig. 24b). This process, which inverts the boron acceptor into a donor unit ($D_{(B)}$) to enhance CT, is termed acceptor-inversion coordination-enhanced CT (iCE-CT). In addition, coordination with an electron-deficient ligand in the A–π–B system yields an A–π–$A_{(B)}$ system.

When the electron-acceptor A is the boron atom (B), the A–π–B can be also represented by B–π–B (Fig. 24c). Recently, boron-based multi-helicene **74a** with superior PLQYs and excellent chiroptical properties was reported by our group (Fig. 25). Upon fluoride titration, the emission of **74a** first bathochromically shifts from green (522 nm) to orange (567 nm) with the formation of mono-fluorinated helicene **74b**, and then hyperchromically shifts to yellow (541 nm) producing a mixture of *cis*/*trans*-di-fluorinated helicene **74c**.[165] This indicates that the titration process from **74a** to **74b** represents a transformation of the B–π–B system into a B–π–$D_{(B)}$ system, where the iCE-CT process results in red-shifted emission. Further transformation to the $D_{(B)}$–π–$D_{(B)}$ system in **74c** leads to blue-shifted emission, resulting from a CQ-CT process (Fig. 24c). Notably, the fluorides in both **74b** and **74c** exhibit negligible contributions to FMOs due to their weak donor ability.

Four-coordinated boron could be dissociable during the photoexcitation process. Yamaguchi and colleagues reported that triarylborane–pyridine complex **75a** underwent a photodissociation process in the excited state, resulting in dual fluorescence (Fig. 26).[166] The shorter-wavelength fluorescence originates from the LE emission of **75a**, while photodissociation in the S_1 state generates uncoordinated borane **75b**, which is responsible for the longer-wavelength emission. Notably, the HOMO of **75a** located at the boron-containing backbone, while the LUMO almost localized on the pyridine group, forming an effective D–π–$A_{(B)}$ system. However, **75a** exhibited a blue-shifted emission to **75b** due to its relatively weaker CT compared to that of **75b**.

Furthermore, we have summarized several representative examples of changes in the CT type and emission wavelength before and after coordination with electron-rich or electron-deficient ligands, and assigned their CT process (Table 1). The CE-CT and CQ-CT mechanisms provide the theoretical foundation both for assigning donor and acceptor roles in tetracoordinate boron molecules and for interpreting FMO analyses, thereby further assisting in understanding the luminescence properties of these molecules.

Since both CE-CT and CQ-CT are caused by the coordination of boron, there could be several prospects and synergies in combining them: (1) by integrating both mechanisms, one can create materials that respond to multiple stimuli. For example, a system that exhibits CE-CT under one set of conditions and CQ-CT under another can be designed to have a more complex and nuanced response profile. This can be particularly useful in creating materials that can adapt to changing environments, such as in adaptive optics or responsive coatings. (2) Combining CE-CT and CQ-CT can lead to materials with tunable emission properties. By carefully designing the coordination environment and the electronic properties of the donor and acceptor moieties, one can achieve a wide range of emission wavelengths and intensities. This can be applied in the development of multi-color emissive materials for displays, lighting, and other applications where a broad color gamut is desired. (3) The ability to switch between CE-CT and CQ-CT can be harnessed to create molecular logic gates. By designing molecules that can

Table 1 Representative examples of changes in the CT type and emission wavelength (λ_{em}) before and after coordination with electron-rich or electron-deficient ligands, and their associated CT processes

Before	CT type[a]	λ_{em}[b] (nm)	Ligand/type	After	CT type[a]	λ_{em}[b] (nm)	(i)CE-CT/CQ-CT	Ref.
74a	B–π–B	522	F^-/D	**74b**	$\mathrm{D_{(B)}}$–π–B	567	iCE-CT	165
74b	$\mathrm{D_{(B)}}$–π–B	567	F^-/D	**74c**	$\mathrm{D_{(B)}}$–π–$\mathrm{D_{(B)}}$	541	CQ-CT	165
75b	$\mathrm{D_{(\pi)}}$–B	550–700	Pyridine/A	**75a**	$\mathrm{D_{(\pi)}}$–$\mathrm{A_{(B)}}$	470–530	—[c]	166
77a	$\mathrm{D_{(\pi)}}$–B	540	–$Ph_2P{=}O$/A	**77b**	$\mathrm{D_{(\pi)}}$–$\mathrm{A_{(B)}}$	440	—[c]	167
78b	D–π–B	511	–NMe_2/D	**78a**	D–π–$\mathrm{D_{(B)}}$	382	CQ-CT	168
79a	D–π–A–B	475	–C=O/A	**79b**	D–π–$\mathrm{A_{(B)}}$	620	CE-CT	169
80a	D–π–B	540	–NHMe/D	**80b**	$\mathrm{D_{(B)}}$–π	—[c]	CQ-CT	170
86a	B–D–A–D–B	485	F^-/D	**86b**	$\mathrm{D_{(B)}}$–D–A–D–$\mathrm{D_{(B)}}$	590	iCE-CT	171

[a] The CT type of these compounds was determined based on the FMO distributions. [b] The emission wavelengths were measured in solution, annealed film, or powder. [c] Not available.

respond to multiple inputs (such as different ligands or environmental conditions) and produce distinct outputs (emission or quenched states), one can develop complex molecular computing systems. This can pave the way for the next generation of molecular electronics and nanoscale computing devices.

5.3 Intramolecular dynamic-coordination induced CT

The coordination bond in tetracoordinate boron compounds is usually dynamic, since it can be formed or cleaved in response to external stimuli, such as temperature, solvent and light. OBCTs can be exploited to construct intramolecular dynamic-coordination systems due to their flexible design enabling stimuli-responsive properties in OBCTs by modulating the ICT process upon coordination. **76a** with an azobenzene photoswitch can be partially converted to the *cis* isomer **76b** upon irradiation, showing an absorption maximum of **76a** at 339 nm while that of **76b** is at 460 nm (Fig. 27a).[172] Wolf *et al.* introduced boron–phosphine oxide Lewis pair systems (**77a** and **77b**) (Fig. 27b).[167] The open structure **77a** is favored in hydrogen-bond-donating (HBD) solvents or at higher temperature, featuring an intense CT fluorescence, while the closed structure **77b** exhibits a 100 nm blue-shifted emission compared to **77a**, attributed to LE transition of **77b**. Introducing mesityl groups on phosphorus impedes the formation of the closed structure due to steric bulk. Subsequently, this system was applied in biological imaging.[173] Analogous to the photo-responsive

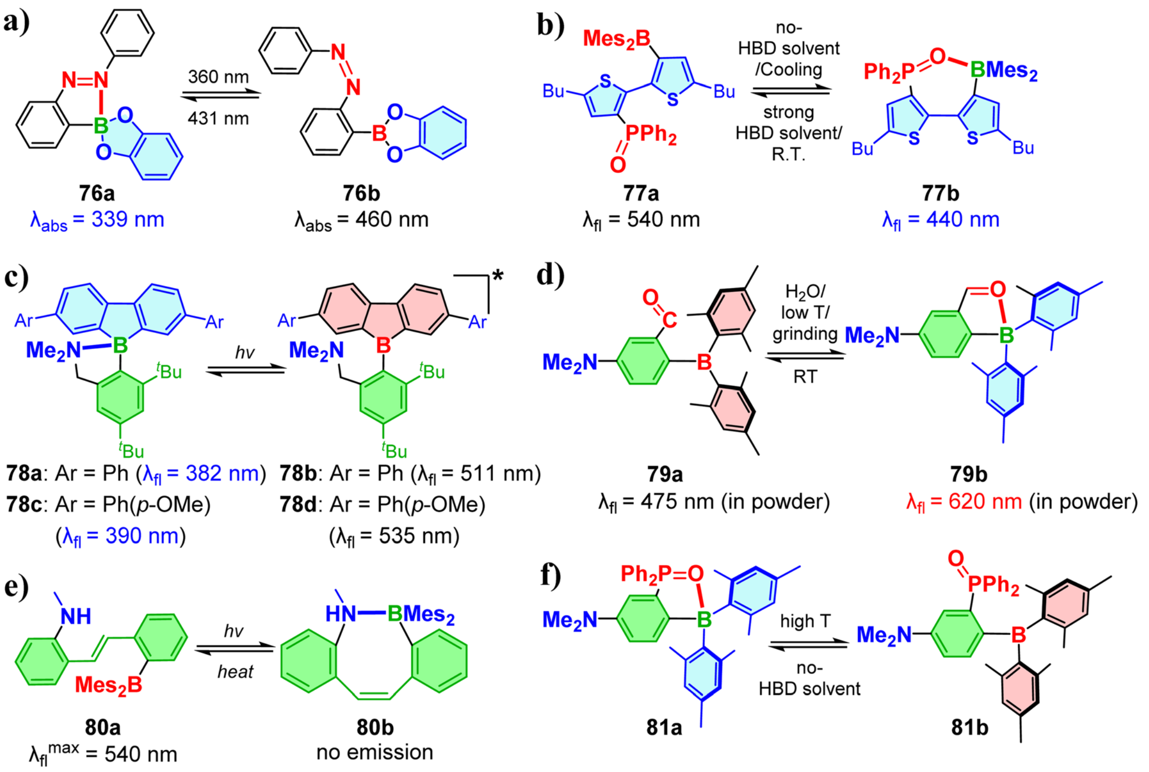

Fig. 27 Intramolecular dynamic coordination systems under external stimuli: (a) **76a** and **76b**; (b) **77a** and **77b**; (c) **78a** and **78b**, **78c** and **78d**; (d) **79a** and **79b**; (e) **80a** and **80b**; (f) **81a** and **81b**.

systems **75a** and **76a**, dibenzoborole derivatives **78a** and **78c** undergo B–N coordination-bond cleavage to form **78b** and **78d** upon photoexcitation (Fig. 27c).[168] This process is termed bond-cleavage-induced intramolecular charge transfer (BICT) and gives rise to dual emissions, where short-wavelength emissions arise from the LE states of **78a** and **78c** and long-wavelength emissions originate from the CT states of **78b** and **78d**. The electron-donating effect of the aryl (Ar) substituent shifts the HOMOs onto dibenzoborole rather than NMe_2, thereby enabling the CT transitions in **78b** and **78d**. In contrast, the unsubstituted molecule exhibits only a single emission, likely because the CT from NMe_2 to dibenzoborole is quenched by nonradiative decay.

Weak or bulky donors and boron acceptors are required to ensure intramolecular dynamic coordination properties. Wang and co-workers synthesized **79a** featuring bulky $BMes_2$ and an aldehyde group as a weak donor, which can be converted to its closed state **79b** in a 92% H_2O/THF solution (Fig. 27d).[169] H_2O molecules could interact with the amino groups in **79a**, reducing its donating ability to boron and thus increasing boron's electrophilicity, while the oxygen atom of H_2O may also interact with the carbonyl group, enhancing its nucleophilicity. Notably, low temperature and grinding facilitate the formation of molecule **79b**, resulting in an emission color shift from blue to red. Subsequently, replacing the aldehyde group with an alkylamino group formed a series of molecules in which the *tert*-butyl-substituted amino group is responsible for the proton-solvent-responsive absorption.[174] The proportion of the closed-state structure increases in proton solvents, reducing the long-wavelength absorption band of the open-state structure. If the ligand is too weak or bulky to form effective coordination bond, there is no dynamic coordination. The stilbene derivative **80a** can undergo the B→NH coordination process and form **80b** upon light irradiation, which leads to a blue shift in the 388 nm absorption peak and quenched fluorescence (Fig. 27e).[170] In contrast, molecules with bulkier nitrogen substituents than those in **80a** exhibit enhanced fluorescence upon irradiation due to a transition from *trans*-ICT to *cis*-ICT, without the formation of coordination bonds. These *cis* isomers could revert to their *trans* forms upon heating. Recently, compounds **81a** with a phosphine oxide group ligand showed that the S_0–S_1 transition of **81a** primarily originates from the HOMO on the NMe_2-Ph/Mes group to the LUMO + 1 localized at oxygen/phenyl groups of the $O{=}PPh_2$ unit as well as the linker Ph unit (Fig. 27f).[175] **81a** can transform into **81b** with a red-shifted absorption in polar solvent. Increasing the temperature also promotes this transformation, showing a nearly 15.7-fold enhancement in fluorescence intensity from 137 K to 340 K. In addition, grinding **81a** powder induces an 18 nm bathochromic shift, with Φ_{PL} increasing from 4.0% to 13.0%.

In addition to dynamic coordination by switching open/closed states, Wang and co-workers reported **82a** with constrained ring systems and an internal dynamic B→N bond (Fig. 28a).[176] The B→N bond length in **82a** (1.80 Å) is longer than the typical B→N bond length (<1.70 Å), and its boron atom adopts a nearly sp^3-hybridized geometry, indicating the formation of a loose B→N bond. Crystals of **82a** exhibits weak emission at ambient temperature, while the emission intensity significantly increases as the temperature rises, due to cleavage of the B→N bond to produce **82b**. Grinding the crystals of **82a** leads to a fluorescence change from blue to green with an increase in emission intensity (Fig. 28b). A similar molecule **83** by changing the substituents on boron and nitrogen exhibited pronounced photochromism upon UV irradiation, switching from short-lived fluorescence to long-lived phosphorescence.[177] In addition, a range of extended dimeric B/N-coordinated molecules **84a–84c** exhibited different ratios of sp^2-and sp^3-hybridized boron by varying the number of methyl substituents on the π-linkers.[178] The HOMO of **84a** localized on the central diaminophenyl linker, while the LUMO delocalized over two $BMes_2$ groups. In contrast, the HOMO of **84b** localized on the tetracoordinated B/N Lewis adduct (sp^3-B), while the LUMO resided on the other Lewis pair unit (sp^2-B) (Fig. 28c). Although the sp^3-B/N dimer **84c** was non-emissive in solution, grinding the solid-state material resulted in a substantial increase in PLQY from 2% to 60%, attributed to the cleavage of the B→N bond.

Similar to the intramolecular dynamic coordination of **79a**/**79b** (Fig. 27d), the open state **85a** exists in a crystalline form or in an annealed film and partially transforms into the closed-shell structure **85b** upon dissolution or in a cast film, accompanied by red-shifted absorption (Fig. 29).[179] The formation of the B→N bond significantly lowers the LUMO level from −1.59 eV in **85a** to −2.29 eV in **85b**, while the HOMO level increases slightly (+0.18 eV). Additionally, the crystals of **85a** change from yellow to dark green upon grinding, likely due to the partial formation of **85b**. Coordinating the boron atom in

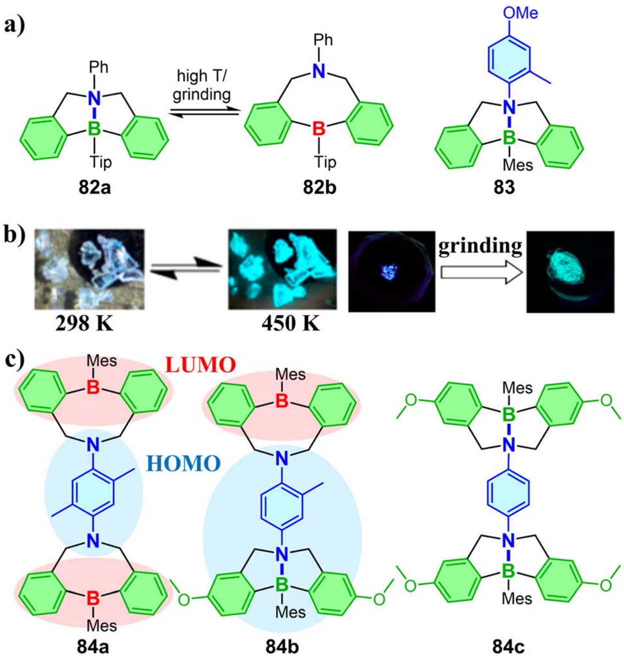

Fig. 28 (a) Single BN system and (c) double BN constrained-ring systems with intramolecular dynamic coordination under external stimuli. (b) Photograph showing the temperature increase- and grinding-driven fluorescence change from the single crystal **82a** to **82b**. Copyright 2018, American Chemical Society.

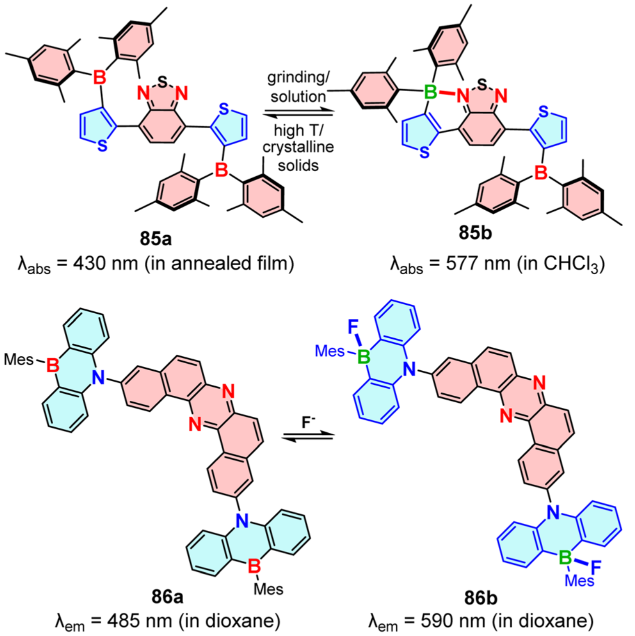

Fig. 29 Molecules with red-shifted emission by changing coordination of boron.

OBCTs with electron-rich ligands could also result in red-shifted absorption and emission, as shown in Fig. 24c. Similarly, **86a** featuring 1,4-phenazaborine as a weak electron donor, exhibits red-shifted emission when its boron atoms coordinate with electron-rich fluoride to form molecule **86b**.[171] This red shift occurs because the weak B–N donor forms a stronger F–B–N donor in **86b**, enhancing the CT from the nitrogen fragment to the dibenzo[*a*,*j*]phenazine (DBPHZ) unit. Through coordination with anions, **86a**-based films achieve tunable photoluminescence ranging from a blue to a deep red–NIR region.

6. Conclusions and perspectives

Organoboron compounds with flexible molecular design are capable of accommodating various CT processes and can be utilized to create innovative CT molecules, in which boron's unique coordination ability forms two distinct systems, three-coordinated and four-coordinated OBCTs. Boron plays a versatile role ranging from an acceptor to a donor–acceptor regulator in these systems. Herein, this perspective has summarized the booming field of three- and four-coordinated OBCTs focusing on several critical aspects: structural design, ICT mechanisms and their impact on optoelectronic properties, as well as the present pros and cons and the future development of OBCTs. Designing desired molecules by exploiting CT mechanisms offers an efficient approach that often leads to remarkable results with less effort. In addition, integrating multiple CT mechanisms or developing novel ones can significantly boost the performance of OBCTs.

Among the extensively reported tricoordinate OBCTs, D–A OBCTs with triarylboryl acceptors are the most prevalent, featuring a CT process that is highly dependent on the arrangements and ratios of donors and acceptors. To better understand and refine the structure–property relationships of D–A OBCTs, it's crucial to carry out further research on additional D–A arrangements and spatial configurations, as well as to modify triarylboryl acceptors by introducing electron-donating or electron-withdrawing groups for OBCTs. Most D–A OBCTs undergo a twist excited state process, termed TICT OBCTs. Flexible TICT OBCTs, featuring freely rotatable single bonds between donors and acceptors, often exhibit dual emissions derived from LE and TICT states. The long-wavelength TICT emission is sensitive to solvent polarity and the ratio of TICT to LE can be increased upon cooling. Designing irreversible conversion from the LE state to the TICT state has significant application potential. By incorporating weak intramolecular interactions within the TICT configuration, the TICT state can be stabilized once formed from the LE state, preventing the reverse process. This process enables a gradual shift from dual emissions to single TICT emission over time, making it ideal for "self-destruct after reading" anti-counterfeiting technologies. Conversely, the stabilized TICT states which can revert to the LE states upon external stimuli might possess potential in molecular solar thermal energy storage (MOST).[180,181] In addition, TICT OBCTs can achieve white-light emission or exhibit multi-stage stimulus-responsive behavior when capable of undergoing further transformations *via* proton transfer and other processes. TICT driven intermolecular interactions can also lead to light-controlled supramolecular self-assembly, broadening their potential for macroscopic applications. Rigid TICT OBCTs, featuring restricted rotation around single bonds between donors and acceptors, can achieve TADF with minimal ΔE_{ST}. However, forbidden transition in these molecules typically results in a low PLQY. Introduction of LE contribution into rigid TICT OBCTs without altering the rigid twisted structure can be achieved through increasing the π-conjugation of donors or acceptors, which paves the way for high-performance OLED devices.

Incorporating π-bridges between donors and acceptors leads to the formation of D–π–A OBCTs, in which the conjugated bridge facilitates LE transition and amplifies the transition dipole moment, while the functional π-bridge such as tetraphenylethene, macrocyclic and pillar[5]arene, or quinoid conjugated motifs can endow D–π–A OBCTs with AIE, chiroptical properties, and NIR emission, respectively. Correspondingly, introducing a donor–acceptor CT process can enhance the luminescence properties of the functional π-bridge. Exploiting azobenzene, spiropyran, or triphenylethylene as photoresponsive functional π-bridges enables the further construction of highly luminescent D–π–A molecular switches and enhances photoreaction rates. Moreover, introducing additional new functional fragments into D–π–A OBCTs is also worthwhile for presenting additional properties. D–π–A OBCTs with several LE transitions could exhibit an HLCT process, where higher triplet excited states are involved in the RISC process, resulting in the effective utilization of triplet excitons. The boron atom provides an optimal HLCT acceptor candidate as it can easily increase LE contributions by combining with π fragments or heteroatom donors. However, reports on HLCT

OBCTs remain scarce, highlighting an untapped area for future exploration.

The boron atom has also been used to design SR-CT molecules. MR-TADF OBCTs utilize the opposing resonance effects of boron and heteroatom donors in the central phenyl rings, to achieve TADF with narrow FWHM emission which can further be red-shifted when combined with B–π–B (LE) or LR-CT strategies. Additionally, TSCT OBCTs with parallel donor–acceptor alignments provide effective coordination, enhance transition dipole moments, and prevent π–π stacking. Meanwhile, rigid TSCT OBCTs also support efficient TADF. To overcome the limitations of existing CT mechanisms and realize innovative CT pathways, it is essential to consider detailed factors, such as resonance effects, the geometry of sp^2-hybridized vacant orbitals of boron, and the spatial configuration of molecules during the molecular design. Developing new CT mechanisms for tricoordinate organoboron compounds is challenging, and thus combining multiple CT mechanisms offers an effective strategy to compensate for individual limitations. For instance, designing molecules with medium-range CT mechanisms[182] can combine the advantages of LR-CT and SR-CT, while alternating donor–acceptor fragments instead of atoms to emulate MR effects could enable narrow-band emission in D–π–A OBCTs.

CT in tetracoordinate boron compounds has been less developed compared to their tricoordinate boron counterparts, which is due to the filled vacant orbitals in the boron atom, complicating the internal CT mechanism. Therefore, tetracoordinate boron OBCTs are typically exploited to be strong electron-withdrawing substituents as acceptor fragments. An in-depth comprehension of diverse mechanisms of tetracoordinate boron can boost the development of OBCTs. Four-coordinated OBCTs demonstrate unique electronic mechanisms, including resonance effects (*e.g.*, B–N and B→N) and hyperconjugation, while boron substituents and chelating ligands can serve as donor and acceptor components to construct TADF molecules. Our group introduced the CE-CT mechanism, which leverages coordination between boron atoms and electron-deficient substituents, paired with covalent donor linkages, to enhance electron push–pull effects and amplify molecular donor–acceptor strengths. In this perspective, we introduce theoretical models of D–π–B, A–π–B, and B–π–B and explore how coordination affects CT properties based on the CE-CT mechanism. Additionally, dynamic intramolecular coordination can achieve stimuli-responsive molecular designs.

While studying the CT mechanisms of tetracoordinate boron, it is crucial to explore the role of chelation: (1) the resonance effect could switch the role of donors and acceptors, that is, the resonance effect might change a donor to an acceptor, and (2) how hyperconjugation resulting from various chelation of boron (*e.g.*, functional groups and geometry configuration) impacts CT. The unique CE-CT induced by tetracoordinate boron allows precise assignment of donor and acceptor segments in the tetracoordinate OBCTs while the boron atom only acts as a regulatory bridge. However, detailed studies on the impact of ligands in CE-CT are essential, as most current tetracoordinate OBCTs exhibit CQ-CT processes, highlighting the imperative for suitable chelating ligand selection. The CT of pentacoordinate boron systems also deserves exploration, since it can form a three-center four-electron (3c-4e) bond.[183] Additionally, the design concept of tricoordinate boron CT can be also used for constructing tetracoordinate OBCTs. For example, constructing D–π–A four-coordinated OBCTs by combining various functional fragments endows molecules with new functions. Alternatively, four-coordinated MR-TADF OBCTs molecules can be designed through CE-CT to achieve highly efficient red and NIR OLEDs. The unique tetrahedral spatial structure of four-coordinated OBCTs is highly suitable for constructing TSCT molecules by changing substituents and constructing TADF molecules with small ΔE_{ST} and high PLQYs. By combining three-coordinated and four-coordinated boron, the CT process can proceed from four-coordinated boron as a donor to three-coordinated boron as an acceptor, and the photophysical properties can be further tuned *via* coordination at the three-coordinated boron.

Not only does the CT mechanism of organoboron compounds and the role played by boron still require further research, but the corresponding application scenarios for OBCTs are also underexplored. Many studies do not explore the corresponding application scenarios or devices after investigating the optoelectronic properties induced by CT. If OBCTs can be used in more practical applications like MR-TADF OLEDs and biological sensing, more attention will be paid to research on OBCTs.

Data availability

No primary research results, software or code have been included and no new data were generated or analysed as part of this review.

Author contributions

All authors contributed to the writing and revision of the manuscript and approved the final version of the perspective.

Conflicts of interest

There are no conflicts to declare.

Acknowledgements

The authors thank the National Natural Science Foundation of China (22001211), the Key Research and Development Program of Shaanxi Province (2023YBGY-454) and the Shaanxi Fundamental Science Research Project for Chemistry & Biology (Grant No. 22JHQ015) for financial support.

References

1 W. Rettig, *Angew. Chem., Int. Ed.*, 1986, **25**, 971–988.
2 R. A. Marcus and N. Sutin, *Biochim. Biophys. Acta, Rev. Bioenerg.*, 1985, **811**, 265–322.

3 R. Misra and S. P. Bhattacharyya, in *Intramolecular Charge Transfer*, ed. R. Misra and S. P. Bhattacharyya, Wiley-VCH, Weinheim, 2018, ch. 2, pp. 29–69, DOI: 10.1002/9783527801916.ch2.
4 X. Chen, X. Zhang, X. Xiao, Z. Wang and J. Zhao, *Angew. Chem., Int. Ed.*, 2023, **62**, e202216010.
5 S. Zeng, X. Liu, Y. S. Kafuti, H. Kim, J. Wang, X. Peng, H. Li and J. Yoon, *Chem. Soc. Rev.*, 2023, **52**, 5607–5651.
6 V. G. Pivovarenko and A. S. Klymchenko, *Chem. Rec.*, 2024, **24**, e202300321.
7 Z.-L. Che, C.-C. Yan, X.-D. Wang and L.-S. Liao, *Chin. J. Chem.*, 2022, **40**, 2468–2481.
8 S. K. Mellerup and S. Wang, *Trends Chem.*, 2019, **1**, 77–89.
9 A. J. T. Lou and T. J. Marks, *Acc. Chem. Res.*, 2019, **52**, 1428–1438.
10 J. Wu, W. Liu, J. Ge, H. Zhang and P. Wang, *Chem. Soc. Rev.*, 2011, **40**, 3483–3495.
11 A. Pal, M. Karmakar, S. R. Bhatta and A. Thakur, *Coord. Chem. Rev.*, 2021, **448**, 214167.
12 C. Chen, C.-Z. Du and X.-Y. Wang, *Adv. Sci.*, 2022, **9**, 2200707.
13 M. Hirai, N. Tanaka, M. Sakai and S. Yamaguchi, *Chem. Rev.*, 2019, **119**, 8291–8331.
14 X. Chen, D. Tan and D.-T. Yang, *J. Mater. Chem. C*, 2022, **10**, 13499–13532.
15 H. Lv, K. Xiang and D.-T. Yang, *Eur. J. Org Chem.*, 2022, **2022**, e202201208.
16 X. Liang and Q. Zhang, *Sci. China Mater.*, 2017, **60**, 1093–1101.
17 L. Wu, M. Holzapfel, A. Schmiedel, F. Peng, M. Moos, P. Mentzel, J. Shi, T. Neubert, R. Bertermann, M. Finze, M. A. Fox, C. Lambert and L. Ji, *Nat. Commun.*, 2024, **15**, 3005.
18 J. Ochi, K. Tanaka and Y. Chujo, *Angew. Chem., Int. Ed.*, 2020, **59**, 9841–9855.
19 Z. Fan, Y. Liu, T. Zhang, Y. Wang and C. Dou, *CCS Chem.*, 2024, 1–10.
20 L. Yuan, J. Yang, S. Qi, Y. Liu, X. Tian, T. Jia, Y. Wang and C. Dou, *Angew. Chem., Int. Ed.*, 2023, **62**, e202314982.
21 Y. Liu, L. Yuan, J. Guo, W. Sun, Y. Wang and C. Dou, *Angew. Chem., Int. Ed.*, 2023, **62**, e202306911.
22 S. S. Kothavale and J. Y. Lee, *Adv. Opt. Mater.*, 2020, **8**, 2000922.
23 J. Guo, Y. Yang, C. Dou and Y. Wang, *J. Am. Chem. Soc.*, 2021, **143**, 18272–18279.
24 W. Zhuang, F.-F. Hung, C.-M. Che and J. Liu, *Angew. Chem., Int. Ed.*, 2024, **63**, e202406497.
25 Y. Xu, Q. Wang, X. Cai, C. Li, S. Jiang and Y. Wang, *Angew. Chem., Int. Ed.*, 2023, **62**, e202312451.
26 D. Li, H. Zhang and Y. Wang, *Chem. Soc. Rev.*, 2013, **42**, 8416–8433.
27 Y. Guo, C. Chen and X.-Y. Wang, *Chin. J. Chem.*, 2023, **41**, 1355–1373.
28 J. Miao, Y. Wang, J. Liu and L. Wang, *Chem. Soc. Rev.*, 2022, **51**, 153–187.
29 S. K. Mellerup and S. Wang, *Chem. Soc. Rev.*, 2019, **48**, 3537–3549.
30 H.-B. Cheng, X. Cao, S. Zhang, K. Zhang, Y. Cheng, J. Wang, J. Zhao, L. Zhou, X.-J. Liang and J. Yoon, *Adv. Mater.*, 2023, **35**, 2207546.
31 Y. Ma, S.-J. Lou and Z. Hou, *Chem. Soc. Rev.*, 2021, **50**, 1945–1967.
32 Q. Xue and G. Xie, *Adv. Opt. Mater.*, 2021, **9**, 2002204.
33 T. Zhang, Y. Xiao, H. Wang, S. Kong, R. Huang, V. Ka-Man Au, T. Yu and W. Huang, *Angew. Chem., Int. Ed.*, 2023, **62**, e202301896.
34 S.-Y. Yang, Y.-K. Qu, L.-S. Liao, Z.-Q. Jiang and S.-T. Lee, *Adv. Mater.*, 2022, **34**, 2104125.
35 G. Meng, H. Dai, Q. Wang, J. Zhou, T. Fan, X. Zeng, X. Wang, Y. Zhang, D. Yang, D. Ma, D. Zhang and L. Duan, *Nat. Commun.*, 2023, **14**, 2394.
36 C. Wang, W. Chi, Q. Qiao, D. Tan, Z. Xu and X. Liu, *Chem. Soc. Rev.*, 2021, **50**, 12656–12678.
37 T. Hatakeyama, K. Shiren, K. Nakajima, S. Nomura, S. Nakatsuka, K. Kinoshita, J. Ni, Y. Ono and T. Ikuta, *Adv. Mater.*, 2016, **28**, 2777–2781.
38 K. Liu, Z. Jiang, R. A. Lalancette, X. Tang and F. Jäkle, *J. Am. Chem. Soc.*, 2022, **144**, 18908–18917.
39 Z. Lei and F. Zhang, *Angew. Chem., Int. Ed.*, 2021, **60**, 16294–16308.
40 Y. Xiao, H. Wang, Z. Xie, M. Shen, R. Huang, Y. Miao, G. Liu, T. Yu and W. Huang, *Chem. Sci.*, 2022, **13**, 8906–8923.
41 H. Uoyama, K. Goushi, K. Shizu, H. Nomura and C. Adachi, *Nature*, 2012, **492**, 234–238.
42 D.-H. Kim, A. D'Aléo, X.-K. Chen, A. D. S. Sandanayaka, D. Yao, L. Zhao, T. Komino, E. Zaborova, G. Canard, Y. Tsuchiya, E. Choi, J. W. Wu, F. Fages, J.-L. Brédas, J.-C. Ribierre and C. Adachi, *Nat. Photonics*, 2018, **12**, 98–104.
43 S. Oda, B. Kawakami, M. Horiuchi, Y. Yamasaki, R. Kawasumi and T. Hatakeyama, *Adv. Sci.*, 2023, **10**, 2205070.
44 M. Mamada, A. Aoyama, R. Uchida, J. Ochi, S. Oda, Y. Kondo, M. Kondo and T. Hatakeyama, *Adv. Mater.*, 2024, **36**, 2402905.
45 X. Cai, Y. Pan, C. Li, L. Li, Y. Pu, Y. Wu and Y. Wang, *Angew. Chem., Int. Ed.*, 2024, **63**, e202408522.
46 Z. Ye, H. Wu, Y. Xu, T. Hua, G. Chen, Z. Chen, X. Yin, M. Huang, K. Xu, X. Song, Z. Huang, X. Lv, J. Miao, X. Cao and C. Yang, *Adv. Mater.*, 2024, **36**, 2308314.
47 X. Luo, Q. Jin, M. Du, D. Wang, L. Duan and Y. Zhang, *Adv. Sci.*, 2024, **11**, 2307675.
48 Y. Xu, P. Xu, D. Hu and Y. Ma, *Chem. Soc. Rev.*, 2021, **50**, 1030–1069.
49 Y. Zhang, D. Zhang, J. Wei, X. Hong, Y. Lu, D. Hu, G. Li, Z. Liu, Y. Chen and L. Duan, *Angew. Chem., Int. Ed.*, 2020, **59**, 17499–17503.
50 X. Chen, D. Tan, J. Dong, T. Ma, Y. Duan and D.-T. Yang, *J. Phys. Chem. Lett.*, 2022, **13**, 10085–10091.
51 J. Dong, L. Zhang, D. Tan, J. Wu, N. Wang, S. K. Mellerup, S. Wang and D.-T. Yang, *Chem. Commun.*, 2021, **57**, 9882–9885.
52 M. Zhao and Q. Miao, *Angew. Chem., Int. Ed.*, 2021, **60**, 21289–21294.

53 C. Chen, J. Lu, Y. Lv, Y. Yan, Q. Sun, A. Narita, K. Müllen and X.-Y. Wang, *Angew. Chem., Int. Ed.*, 2022, **61**, e202212594.

54 W. Li, C.-Z. Du, X.-Y. Chen, L. Fu, R.-R. Gao, Z.-F. Yao, J.-Y. Wang, W. Hu, J. Pei and X.-Y. Wang, *Angew. Chem., Int. Ed.*, 2022, **61**, e202201464.

55 S. Zhou, Y. Liu, W. Jin, T. Qin, X. Liu, C. Zhao, Z. Liu and X. Yu, *Org. Lett.*, 2023, **25**, 1573–1577.

56 Y. Zhang, W. Li, R. Jiang, L. Zhang, Y. Li, X. Xu and X. Liu, *J. Org. Chem.*, 2022, **87**, 12986–12996.

57 Y. Yu, L. Wang, D. Lin, S. Rana, K. S. Mali, H. Ling, L. Xie, S. De Feyter and J. Liu, *Angew. Chem., Int. Ed.*, 2023, **62**, e202303335.

58 L. Chen, J. Dong, D. Tan, J. Wu and D.-T. Yang, *Chin. J. Chem.*, 2024, **42**, 3069–3074.

59 T. Ma, J. Dong and D.-T. Yang, *Chem. Commun.*, 2023, **59**, 13679–13689.

60 Y. Yu, C. Wang, F.-F. Hung, C. Chen, D. Pan, C.-M. Che and J. Liu, *J. Am. Chem. Soc.*, 2024, **146**, 22600–22611.

61 T. Kushida, S. Shirai, N. Ando, T. Okamoto, H. Ishii, H. Matsui, M. Yamagishi, T. Uemura, J. Tsurumi, S. Watanabe, J. Takeya and S. Yamaguchi, *J. Am. Chem. Soc.*, 2017, **139**, 14336–14339.

62 M. Ito, S. Shirai, Y. Xie, T. Kushida, N. Ando, H. Soutome, K. J. Fujimoto, T. Yanai, K. Tabata, Y. Miyata, H. Kita and S. Yamaguchi, *Angew. Chem., Int. Ed.*, 2022, **61**, e202201965.

63 Y. H. Lee, W. Lee, T. Lee, D. Lee, J. Jung, S. Yoo and M. H. Lee, *ACS Appl. Mater. Interfaces*, 2021, **13**, 45778–45788.

64 A. Michaelis, A. Michaelis and H. v. Soden, *Liebigs Ann. Chem.*, 1885, **229**, 295–334.

65 P. J. Grisdale, J. L. R. Williams, M. E. Glogowski and B. E. Babb, *J. Org. Chem.*, 1971, **36**, 544–549.

66 J. C. Doty, B. Babb, P. J. Grisdale, M. Glogowski and J. L. R. Williams, *J. Organomet. Chem.*, 1972, **38**, 229–236.

67 R. Stahl, C. Lambert, C. Kaiser, R. Wortmann and R. Jakober, *Chem.–Eur. J.*, 2006, **12**, 2358–2370.

68 A. Proń, M. Baumgarten and K. Müllen, *Org. Lett.*, 2010, **12**, 4236–4239.

69 C.-C. Tsai, W.-C. Huang, H.-Y. Chih, Y.-C. Hsh, C.-W. Liao, C.-H. Lin, Y.-X. Kang, C.-H. Chang, Y. J. Chang and C.-W. Lu, *Org. Electron.*, 2018, **63**, 166–174.

70 Y. Liu, G. Xie, K. Wu, Z. Luo, T. Zhou, X. Zeng, J. Yu, S. Gong and C. Yang, *J. Mater. Chem. C*, 2016, **4**, 4402–4407.

71 Y. Liu, H. Huang, T. Zhou, K. Wu, M. Zhu, J. Yu, G. Xie and C. Yang, *J. Mater. Chem. C*, 2019, **7**, 4778–4783.

72 C. Qu, G. Xia, Y. Xu, Y. Zhu, J. Liang, H. Zhang, J. Wang, Z. Zhang and Y. Wang, *J. Mater. Chem. C*, 2020, **8**, 3846–3854.

73 D. Zhong, S. Liu, L. Yue, Z. Feng, H. Wang, P. Yang, B. Su, X. Yang, Y. Sun and G. Zhou, *Chem. Sci.*, 2024, **15**, 9112–9119.

74 E. Lippert, W. LÜDer and H. Boos, in *Proceedings of the IVth International Meeting on Molecular Spectroscopy*, ed. A. Mangini, Pergamon, 1962, vol. 1, DOI: **10.1016/B978-1-4832-1332-3.50070-6**.

75 K. Rotkiewicz, K. H. Grellmann and Z. R. Grabowski, *Chem. Phys. Lett.*, 1973, **19**, 315–318.

76 J. Feng, K. Tian, D. Hu, S. Wang, S. Li, Y. Zeng, Y. Li and G. Yang, *Angew. Chem., Int. Ed.*, 2011, **50**, 8072–8076.

77 X. Liu, S. Li, J. Feng, Y. Li and G. Yang, *Chem. Commun.*, 2014, **50**, 2778–2780.

78 T. Taniguchi, J. Wang, S. Irle and S. Yamaguchi, *Dalton Trans.*, 2013, **42**, 620–624.

79 C. Arivazhagan, A. Maity, K. Bakthavachalam, A. Jana, S. K. Panigrahi, E. Suresh, A. Das and S. Ghosh, *Chem.–Eur. J.*, 2017, **23**, 7046–7051.

80 Y.-J. Lien, T.-C. Lin, C.-C. Yang, Y.-C. Chiang, C.-H. Chang, S.-H. Liu, Y.-T. Chen, G.-H. Lee, P.-T. Chou, C.-W. Lu and Y. Chi, *ACS Appl. Mater. Interfaces*, 2017, **9**, 27090–27101.

81 P. Ganesan, D.-G. Chen, W.-C. Chen, P. Gnanasekaran, J.-A. Lin, C.-Y. Huang, M.-C. Chen, C.-S. Lee, P.-T. Chou and Y. Chi, *J. Mater. Chem. C*, 2020, **8**, 4780–4788.

82 D. Pecorari, A. Mazzanti, S. Gianvittorio, S. Foschi, S. Stagni, V. Fiorini and M. Mancinelli, *Org. Chem. Front.*, 2021, **8**, 4496–4507.

83 D. Pecorari, E. Giuliani, A. Mazzanti, S. Stagni, V. Fiorini, G. Vigarani, F. Zinna, G. Pescitelli and M. Mancinelli, *J. Org. Chem.*, 2023, **88**, 871–881.

84 M. Numata, T. Yasuda and C. Adachi, *Chem. Commun.*, 2015, **51**, 9443–9446.

85 Y. Kitamoto, T. Namikawa, D. Ikemizu, Y. Miyata, T. Suzuki, H. Kita, T. Sato and S. Oi, *J. Mater. Chem. C*, 2015, **3**, 9122–9130.

86 K. Suzuki, S. Kubo, K. Shizu, T. Fukushima, A. Wakamiya, Y. Murata, C. Adachi and H. Kaji, *Angew. Chem., Int. Ed.*, 2015, **54**, 15231–15235.

87 I. S. Park, K. Matsuo, N. Aizawa and T. Yasuda, *Adv. Funct. Mater.*, 2018, **28**, 1802031.

88 K. Matsuo and T. Yasuda, *Chem. Sci.*, 2019, **10**, 10687–10697.

89 D. H. Ahn, H. Lee, S. W. Kim, D. Karthik, J. Lee, H. Jeong, J. Y. Lee and J. H. Kwon, *ACS Appl. Mater. Interfaces*, 2019, **11**, 14909–14916.

90 T.-L. Wu, M.-J. Huang, C.-C. Lin, P.-Y. Huang, T.-Y. Chou, R.-W. Chen-Cheng, H.-W. Lin, R.-S. Liu and C.-H. Cheng, *Nat. Photonics*, 2018, **12**, 235–240.

91 T. Agou, K. Matsuo, R. Kawano, I. S. Park, T. Hosoya, H. Fukumoto, T. Kubota, Y. Mizuhata, N. Tokitoh and T. Yasuda, *ACS Mater. Lett.*, 2019, **2**, 28–34.

92 Q. Chen, Y. Xiang, X. Yin, K. Hu, Y. Li, X. Cheng, Y. Liu, G. Xie and C. Yang, *Dyes Pigm.*, 2021, **188**, 109157.

93 J. Wang, N. Li, Q. Chen, Y. Xiang, X. Zeng, S. Gong, Y. Zou and Y. Liu, *Chem. Eng. J.*, 2022, **450**, 137805.

94 Y. H. Lee, Y.-S. Shin, T. Lee, J. Jung, J.-H. Lee and M. H. Lee, *Chem. Eng. J.*, 2021, **423**, 130224.

95 G. Xia, C. Qu, Y. Zhu, J. Ye, K. Ye, Z. Zhang and Y. Wang, *Angew. Chem., Int. Ed.*, 2021, **60**, 9598–9603.

96 X. Gong, W. Yang, H. Zhang, W. Ning, S. Gong, X. Gao and C. Yang, *Sci. China Mater.*, 2024, **67**, 3537–3542.

97 Y.-W. Chen, C.-C. Tsai, H.-Y. Chih, H.-Y. Tsai, W.-Y. Wang, G.-Y. Liu, M.-Y. Wu, C.-H. Chang and C.-W. Lu, *Dyes Pigm.*, 2022, **197**, 109892.

98 Y. Shirota, M. Kinoshita, T. Noda, K. Okumoto and T. Ohara, *J. Am. Chem. Soc.*, 2000, **122**, 11021–11022.

99 C.-H. Zhao, A. Wakamiya, Y. Inukai and S. Yamaguchi, *J. Am. Chem. Soc.*, 2006, **128**, 15934–15935.

100 Z. Zhang, R. M. Edkins, J. Nitsch, K. Fucke, A. Eichhorn, A. Steffen, Y. Wang and T. B. Marder, *Chem.–Eur. J.*, 2015, **21**, 177–190.

101 M. Ito, E. Ito, M. Hirai and S. Yamaguchi, *J. Org. Chem.*, 2018, **83**, 8449–8456.

102 H. Shi, D. Xin, S.-D. Bai, L. Fang, X.-E. Duan, J. Roose, H. Peng, S. Chen and B. Z. Tang, *Org. Electron.*, 2016, **33**, 78–87.

103 G. Turkoglu and T. Ozturk, *Dalton Trans.*, 2022, **51**, 2715–2725.

104 J. Jin, Y. Tao, H. Jiang, R. Chen, G. Xie, Q. Xue, C. Tao, L. Jin, C. Zheng and W. Huang, *Adv. Sci.*, 2018, **5**, 1800292.

105 O. S. Ipek, S. Topal and T. Ozturk, *Dyes Pigm.*, 2021, **192**, 109458.

106 R. Oshimizu, N. Ando and S. Yamaguchi, *Angew. Chem., Int. Ed.*, 2022, **61**, e202209394.

107 P. Chen, R. A. Lalancette and F. Jäkle, *Angew. Chem., Int. Ed.*, 2012, **51**, 7994–7998.

108 P. Chen, X. Yin, N. Baser-Kirazli and F. Jäkle, *Angew. Chem., Int. Ed.*, 2015, **54**, 10768–10772.

109 A. Ito, M. Uebe, R. Kurata, S. Yano, H. Fueno and T. Matsumoto, *Chem.–Asian J.*, 2018, **13**, 754–760.

110 J.-F. Chen, X. Yin, B. Wang, K. Zhang, G. Meng, S. Zhang, Y. Shi, N. Wang, S. Wang and P. Chen, *Angew. Chem., Int. Ed.*, 2020, **59**, 11267–11272.

111 P. Li, D. Shimoyama, N. Zhang, Y. Jia, G. Hu, C. Li, X. Yin, N. Wang, F. Jäkle and P. Chen, *Angew. Chem., Int. Ed.*, 2022, **61**, e202200612.

112 Y. Jia, P. Li, K. Liu, C. Li, M. Liu, J. Di, N. Wang, X. Yin, N. Zhang and P. Chen, *Chem. Sci.*, 2022, **13**, 11672–11679.

113 F. Zhao, J. Zhao, H. Liu, Y. Wang, J. Duan, C. Li, J. Di, N. Zhang, X. Zheng and P. Chen, *J. Am. Chem. Soc.*, 2023, **145**, 10092–10103.

114 R. Kurata, A. Ito, M. Gon, K. Tanaka and Y. Chujo, *J. Org. Chem.*, 2017, **82**, 5111–5121.

115 J. Merz, J. Fink, A. Friedrich, I. Krummenacher, H. H. Al Mamari, S. Lorenzen, M. Haehnel, A. Eichhorn, M. Moos, M. Holzapfel, H. Braunschweig, C. Lambert, A. Steffen, L. Ji and T. B. Marder, *Chem.–Eur. J.*, 2017, **23**, 13164–13180.

116 Z.-B. Sun, J.-K. Liu, D.-F. Yuan, Z.-H. Zhao, X.-Z. Zhu, D.-H. Liu, Q. Peng and C.-H. Zhao, *Angew. Chem., Int. Ed.*, 2019, **58**, 4840–4846.

117 M. Uebe, D. Sakamaki and A. Ito, *ChemPlusChem*, 2019, **84**, 1305–1313.

118 M. Ito, M. Sakai, N. Ando and S. Yamaguchi, *Angew. Chem., Int. Ed.*, 2021, **60**, 21853–21859.

119 T. Jairam and W. P. Hong, *J. Mater. Chem. C*, 2022, **10**, 16173–16217.

120 W. Li, Y. Pan, R. Xiao, Q. Peng, S. Zhang, D. Ma, F. Li, F. Shen, Y. Wang, B. Yang and Y. Ma, *Adv. Funct. Mater.*, 2014, **24**, 1609–1614.

121 W. Li, D. Liu, F. Shen, D. Ma, Z. Wang, T. Feng, Y. Xu, B. Yang and Y. Ma, *Adv. Funct. Mater.*, 2012, **22**, 2797–2803.

122 P. Jin, Y. Han, F. Tian, L. Wang, X. Zhao, C. Zhang and J. Xiao, *Chem.–Eur. J.*, 2020, **26**, 3113–3118.

123 Z. Lu, D. Hu, S.-W. Chen, R. Wang, L. Xing, Y. Zhu, J. Lin, Y. Huo and S. Ji, *J. Mater. Chem. C*, 2024, **12**, 9929–9938.

124 J. Lv, J. Li, S. Wang, H. Shen, L. Xia, Y. Liu, S. Xue, D. Ma, S. Ying and S. Yan, *J. Mater. Chem. C*, 2024, **12**, 17475–17481.

125 X.-Q. Gan, Z.-M. Ding, D.-H. Liu, W.-Q. Zheng, B. Ma, H. Zhang, X. Chang, L. Wang, Y. Liu, X. Wu, S.-J. Su and W. Zhu, *Adv. Opt. Mater.*, 2023, **11**, 2300195.

126 R. Wu, K. Sun, G. Shi, Y. Han, T. Gong, Y. Xu, S.-T. Zhang and B. Yang, *Adv. Funct. Mater.*, 2024, **34**, 2403501.

127 G. Li, K. Xu, J. Zheng, X. Fang, W. Lou, F. Zhan, C. Deng, Y.-F. Yang, Q. Zhang and Y. She, *J. Am. Chem. Soc.*, 2024, **146**, 1667–1680.

128 H. Hirai, K. Nakajima, S. Nakatsuka, K. Shiren, J. Ni, S. Nomura, T. Ikuta and T. Hatakeyama, *Angew. Chem., Int. Ed.*, 2015, **54**, 13581–13585.

129 Y. Zhang, D. Zhang, J. Wei, Z. Liu, Y. Lu and L. Duan, *Angew. Chem., Int. Ed.*, 2019, **58**, 16912–16917.

130 Y. Xu, Z. Cheng, Z. Li, B. Liang, J. Wang, J. Wei, Z. Zhang and Y. Wang, *Adv. Opt. Mater.*, 2020, **8**, 1902142.

131 M. Mamada, M. Hayakawa, J. Ochi and T. Hatakeyama, *Chem. Soc. Rev.*, 2024, **53**, 1624–1692.

132 H. J. Kim and T. Yasuda, *Adv. Opt. Mater.*, 2022, **10**, 2201714.

133 C. Lv, X. Wang, Q. Zhang and Y. Zhang, *Mater. Chem. Front.*, 2023, **7**, 2809–2827.

134 M. Yang, I. S. Park and T. Yasuda, *J. Am. Chem. Soc.*, 2020, **142**, 19468–19472.

135 P. Keerthika and R. K. Konidena, *Adv. Opt. Mater.*, 2023, **11**, 2301732.

136 Y. Kondo, K. Yoshiura, S. Kitera, H. Nishi, S. Oda, H. Gotoh, Y. Sasada, M. Yanai and T. Hatakeyama, *Nat. Photonics*, 2019, **13**, 678–682.

137 M. Hayakawa, X. Tang, Y. Ueda, H. Eguchi, M. Kondo, S. Oda, X.-C. Fan, G. N. Iswara Lestanto, C. Adachi and T. Hatakeyama, *J. Am. Chem. Soc.*, 2024, **146**, 18331–18340.

138 X. Y. Liu, D. R. Bai and S. Wang, *Angew. Chem., Int. Ed.*, 2006, **45**, 5475–5478.

139 D.-R. Bai, X.-Y. Liu and S. Wang, *Chem.–Eur. J.*, 2007, **13**, 5713–5723.

140 Z. M. Hudson, X.-Y. Liu and S. Wang, *Org. Lett.*, 2011, **13**, 300–303.

141 H. Pan, G.-L. Fu, Y.-H. Zhao and C.-H. Zhao, *Org. Lett.*, 2011, **13**, 4830–4833.

142 M.-Y. Zhang, Z.-Y. Li, B. Lu, Y. Wang, Y.-D. Ma and C.-H. Zhao, *Org. Lett.*, 2018, **20**, 6868–6871.

143 Y. H. Lee, S. Park, J. Oh, J. W. Shin, J. Jung, S. Yoo and M. H. Lee, *ACS Appl. Mater. Interfaces*, 2017, **9**, 24035–24042.

144 Y. H. Lee, S. Park, J. Oh, S.-J. Woo, A. Kumar, J.-J. Kim, J. Jung, S. Yoo and M. H. Lee, *Adv. Opt. Mater.*, 2018, **6**, 1800385.

145 A. Kumar, W. Lee, T. Lee, J. Jung, S. Yoo and M. H. Lee, *J. Mater. Chem. C*, 2020, **8**, 4253–4263.

146 X.-L. Chen, J.-H. Jia, R. Yu, J.-Z. Liao, M.-X. Yang and C.-Z. Lu, *Angew. Chem., Int. Ed.*, 2017, **56**, 15006–15009.

147 M. Ouyang, L. Xing, Q. Chen, H. Huang, M. Zhu, K. Hu, Y. Liu, W.-C. Chen, Y. Huo and C. Yang, *J. Mater. Chem. C*, 2021, **9**, 1678–1684.
148 C. Wu, W. Liu, K. Li, G. Cheng, J. Xiong, T. Teng, C.-M. Che and C. Yang, *Angew. Chem., Int. Ed.*, 2021, **60**, 3994–3998.
149 B. Du, X. Wang, F. Chen, Q. Yang, S. Shao, L. Wang, X. Jing and F. Wang, *Chem. Commun.*, 2021, **57**, 7144–7147.
150 Z. Zhao, C. Zeng, X. Peng, Y. Liu, H. Zhao, L. Hua, S.-J. Su, S. Yan and Z. Ren, *Angew. Chem., Int. Ed.*, 2022, **61**, e202210864.
151 P. Zuo, Y.-J. Yang, F.-M. Liu, J.-R. Wu, Q. Zheng, H.-T. Yuan, L.-S. Liao, D.-Y. Zhou and Z.-Q. Jiang, *Adv. Opt. Mater.*, 2024, **12**, 2400860.
152 S. Luo, J. Wang, N. Li, X.-F. Song, X. Wan, K. Li and C. Yang, *Angew. Chem., Int. Ed.*, 2023, **62**, e202310943.
153 X.-F. Luo, L. Shen, J.-Y. Wang and X. Xiao, *Chem. Commun.*, 2024, **60**, 574–577.
154 A. Kumar, H. Y. Shin, T. Lee, J. Jung, B. J. Jung and M. H. Lee, *Chem.–Eur. J.*, 2020, **26**, 16793–16801.
155 H. Narita, H. Min, N. Kubo, I. Hattori, T. Yasuda and S. Yamaguchi, *Angew. Chem., Int. Ed.*, 2024, **63**, e202405412.
156 Y.-L. Rao and S. Wang, *Inorg. Chem.*, 2011, **50**, 12263–12274.
157 A. C. Murali, P. Nayak and K. Venkatasubbaiah, *Dalton Trans.*, 2022, **51**, 5751–5771.
158 X. Shao, M. Liu, J. Liu and L. Wang, *Angew. Chem., Int. Ed.*, 2022, **61**, e202205893.
159 C. Zhu, X. Ji, D. You, T. L. Chen, A. U. Mu, K. P. Barker, L. M. Klivansky, Y. Liu and L. Fang, *J. Am. Chem. Soc.*, 2018, **140**, 18173–18182.
160 Y.-J. Shiu, Y.-C. Cheng, W.-L. Tsai, C.-C. Wu, C.-T. Chao, C.-W. Lu, Y. Chi, Y.-T. Chen, S.-H. Liu and P.-T. Chou, *Angew. Chem., Int. Ed.*, 2016, **55**, 3017–3021.
161 L. Zhou, F. Ni, N. Li, K. Wang, G. Xie and C. Yang, *Angew. Chem., Int. Ed.*, 2022, **61**, e202203844.
162 L. Jiang, Y. Wang, D. Tan, X. Chen, T. Ma, B. Zhang and D.-T. Yang, *Chem. Sci.*, 2022, **13**, 5597–5605.
163 D.-T. Yang, T. Nakamura, Z. He, X. Wang, A. Wakamiya, T. Peng and S. Wang, *Org. Lett.*, 2018, **20**, 6741–6745.
164 J. Dong, L. Chen, Q. Feng and D. Yang, *Angew. Chem., Int. Ed.*, 2025, **64**, e202417200.
165 D. Tan, J. Dong, T. Ma, Q. Feng, S. Wang and D.-T. Yang, *Angew. Chem., Int. Ed.*, 2023, **62**, e202304711.
166 K. Matsuo, S. Saito and S. Yamaguchi, *J. Am. Chem. Soc.*, 2014, **136**, 12580–12583.
167 Y. Cao, J. K. Nagle, M. O. Wolf and B. O. Patrick, *J. Am. Chem. Soc.*, 2015, **137**, 4888–4891.
168 T. Matsumoto, K. Tanaka, K. Tanaka and Y. Chujo, *Dalton Trans.*, 2015, **44**, 8697–8707.
169 Y.-g. Shi, J.-w. Wang, H. Li, G.-f. Hu, X. Li, S. K. Mellerup, N. Wang, T. Peng and S. Wang, *Chem. Sci.*, 2018, **9**, 1902–1911.
170 G. Ji, N. Wang, X. Yin and P. Chen, *Org. Lett.*, 2020, **22**, 5758–5762.
171 N. Aota, R. Nakagawa, L. E. de Sousa, N. Tohnai, S. Minakata, P. de Silva and Y. Takeda, *Angew. Chem., Int. Ed.*, 2024, **63**, e202405158.
172 N. Kano, J. Yoshino and T. Kawashima, *Org. Lett.*, 2005, **7**, 3909–3911.
173 Y. Cao, X. Wang, X. Shi, S. M. Clee, P. L. McGeer, M. O. Wolf and C. Orvig, *Angew. Chem., Int. Ed.*, 2017, **56**, 15603–15606.
174 H.-J. Li, S. K. Mellerup, X. Wang and S. Wang, *Org. Lett.*, 2019, **21**, 2838–2842.
175 Y. Wang, K. Liu, P. Chen, X. Yin, T. Peng, J. Iqbal and N. Wang, *J. Mater. Chem. C*, 2022, **10**, 10981–10987.
176 Q. Hou, L. Liu, S. K. Mellerup, N. Wang, T. Peng, P. Chen and S. Wang, *Org. Lett.*, 2018, **20**, 6467–6470.
177 Y. Shi, Y. Zeng, P. Kucheryavy, X. Yin, K. Zhang, G. Meng, J. Chen, Q. Zhu, N. Wang, X. Zheng, F. Jäkle and P. Chen, *Angew. Chem., Int. Ed.*, 2022, **61**, e202213615.
178 Y. Shi, C. Li, H. Ma, Z. Cao, K. Liu, X. Yin, N. Wang and P. Chen, *Org. Lett.*, 2022, **24**, 5497–5502.
179 H. Shimogawa, O. Yoshikawa, Y. Aramaki, M. Murata, A. Wakamiya and Y. Murata, *Chem.–Eur. J.*, 2017, **23**, 3784–3791.
180 Z. Wang, H. Hölzel and K. Moth-Poulsen, *Chem. Soc. Rev.*, 2022, **51**, 7313–7326.
181 R. C. Richter, S. M. Biebl, R. Einholz, J. Walz, C. Maichle-Mössmer, M. Ströbele, H. F. Bettinger and I. Fleischer, *Angew. Chem., Int. Ed.*, 2024, **63**, e202405818.
182 X. He, J. Lou, B. Li, X. Dong, F. Zhong, W. Liu, X. Feng, D. Yang, D. Ma, Z. Zhao, Z. Wang and B. Z. Tang, *Adv. Mater.*, 2024, **36**, 2310417.
183 C. Dou, S. Saito and S. Yamaguchi, *J. Am. Chem. Soc.*, 2013, **135**, 9346–9349.